

Field validation and benchmarking of a cloud shadow speed sensor

P. Kuhn^{1,*}

Paseo de Almería 73, 04001 Almería, Spain

M. Wirtz¹, S. Wilbert¹, J. L. Bosch², G. Wang³, L. Ramirez⁴, D. Heinemann⁵,
R. Pitz-Paal⁶

Abstract

With ramp rate regulations for photovoltaic plants being discussed in many countries, the speed of clouds has gained significant importance lately. Besides, measuring cloud velocities and directions is of interest for validations of numerical weather predictions and solar nowcasting systems. Recently, the Cloud Shadow Speed Sensor (CSS) was developed and validated in San Diego for low cumulus clouds. In this publication, the CSS is studied under different weather and cloud conditions in the desert of Tabernas in southern Spain. Furthermore, a novel shadow camera based low-cost, low-maintenance approach to determine cloud shadow motion vectors is presented and used as a reference to benchmark the CSS. In comparison, the absolute velocities derived from the CSS and the shadow camera on 59 days for ± 5 min temporal medians show deviations of

*Corresponding author

Email address: `Pascal.Kuhn@dlr.de` (P. Kuhn)

¹German Aerospace Center (DLR), Institute of Solar Research, Paseo de Almería 73, 04001 Almería, Spain.

²Departamento de Ingeniería Eléctrica y Térmica, Universidad de Huelva, Campus de La Rábida, Carretera de Palos de la Frontera S/N 21071 La Rábida, Palos de la Frontera (Huelva)

³Dept of Mechanical and Aerospace Engineering, UCSD Center for Energy Research, University of California, 92093-0411 La Jolla, USA.

⁴CIEMAT, Energy Department - Renewable Energy Division. Av. Complutense, 40, 28040 Madrid, Spain.

⁵Energy Meteorology Unit, Energy and Semiconductor Research Laboratory, Institute of Physics - Oldenburg University, 26111 Oldenburg, Germany.

⁶German Aerospace Center (DLR), Institute of Solar Research, Linder Höhe, 51147 Cologne, Germany.

RMSD 2.1 m/s (28.0 %), MAD 1.2 m/s (15.7 %) and a bias of -0.2 m/s (2.8 %). Deviations of the cloud shadow direction are RMSD 47.9° (26.6 %), MAD 25.3° (14.0 %) and bias 3.7° (2.0 %). An adaption of the CSS software yields 91 % more measurements on 59 days in comparison to the previously used algorithms at the expense of reduced accuracies, both for the measured velocities and for the measured directions.

The CSS and the novel shadow camera based reference system enable long-time, low-maintenance ground measurements of cloud shadow speeds, which were previously not available. The distinct advantages and limitations of the two systems are discussed. In addition to the comparisons between the shadow camera system and the CSS on 59 days, the detection rates of the CSS are classified and measured on 223 days by analyzing CSS radiometer signals. Depending on the shading strength and shading durations, detection rates vary between 3.7 % and 21.6 %. Furthermore, the basic assumption as well as possible correction approaches of the linear cloud edge - curve fitting method are studied.

The CSS was found to be a robust tool with great potential. However, optically thin clouds with diffuse edges pose a challenge and the detection rate leaves room for improvements. The newly developed shadow camera system provides more measurements which scatter less but needs certain geographical requirements. The shadow camera is found to be a feasible validation tool for cloud (shadow) motion vectors.

Keywords: Cloud shadow speed sensor, cloud speed, shadow camera system

1. Introduction

Obtaining reference motion vectors of clouds is relevant for the optimization and validation of all-sky imager based nowcasting systems (Kuhn et al., 2017a) as well as numerical weather predictions (NWP) and satellite-based weather forecasts (Molteni et al. (1996), Klein and Jakob (1999), Tomassini et al. (1999)). In addition to that, the rapid growth of solar power generation with its inherent

7 variability calls for solar forecasting tools, which can predict shading events.
8 Recently, ramp rate regulations (Lave et al. (2013), Marcos et al. (2014), Chen
9 et al. (2017)) in several countries with high solar grid penetrations have further
10 stressed the need of cloud speed measurements. The Cloud Shadow Speed
11 Sensor (CSS) can be used to derive such cloud motion vectors and can be a part
12 of a camera-based solar nowcasting system (Wang et al., 2016). A singular all-
13 sky imager can measure angular speeds of clouds, but cannot provide absolute
14 speeds in [m/s].

15 The CSS, pictured in Fig. 1, was developed and presented in Fung et al.
16 (2013). Previous validations, both under laboratory conditions and in-field,
17 have been conducted (Fung et al., 2013). However, the variability of clouds
18 and the complexity of the weather vary for different locations. For instance, in
19 San Diego (USA), where the CSS was previously validated, cloud heights rarely
20 exceed 1000 m (Wang et al., 2016).

21 In this publication, the CSS is compared to a novel shadow camera reference
22 system on 59 days at the Plataforma Solar de Almería (PSA) in southern Spain.
23 In southern Spain, a wide range of cloud speeds, heights and clouds of various
24 classes is observed (Killius et al. (2015), Kuhn et al. (2017a)). Investigating
25 and benchmarking the performance of the CSS in this complex meteorological
26 environment gives insights into its general applicability. In addition to the
27 comparison against a shadow camera on 59 days, the detection rate of the CSS

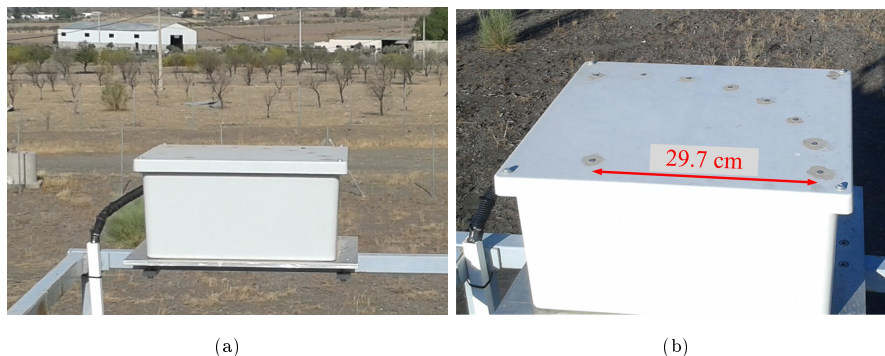


Figure 1: The Cloud Shadow Speed Sensor (CSS) at PSA, Spain.

28 is determined on 223 days by directly investigating the measurements of the
29 CSS sensors.

30 The shadow camera is a downward-facing camera placed on top of an 87 m
31 high tower (CIEMAT CESA-I), which is part of a shadow camera system pro-
32 viding spatially resolved irradiance maps (Kuhn et al. (2017a), Kuhn et al.
33 (2017b), Kuhn et al. (2017c), Kuhn et al. (2018a)). The shadow camera is used
34 to measure reference cloud speeds, which are compared to the CSS.

35 This publication is structured as follows. After the introduction, the CSS is
36 presented and its software optimization discussed in section 2. In section 3, the
37 shadow camera method is explained in detail. Comparing these two systems
38 in section 4 enables an in-field validation of the CSS. Also, the detection rate
39 is determined in this section by scrutinizing the raw data of the CSS. The
40 advantages and disadvantages of the CSS in comparison with the shadow camera
41 approach are discussed in section 5. The conclusion is given in section 6. In
42 the appendix, assumptions and possible corrections of the Linear Cloud Edge
43 method are studied.

44 **2. The Cloud Shadow Speed Sensor**

45 *2.1. Working principle*

46 The working principle of the CSS, developed by Fung et al. (2013), is based
47 on methods for determining cloud motion vectors with an array of irradiance
48 sensors (Bosch and Kleissl (2013), Bosch et al. (2013), Schenk et al. (2015)). It
49 consists of nine uncalibrated photodiode pyranometers, which are sampled at
50 a frequency of 667 s^{-1} . Eight of these sensors are placed in a circular arc of
51 105° with a radius of 29.7 cm around the ninth sensor (see Fig. 1). In order to
52 measure the speed and direction of a cloud shadow, the CSS must be directly
53 shaded. If the shadow of a cloud passes the CSS, the sensors detect ramps at
54 slightly different times. This way, both the speed and the direction of the clouds
55 is determined. Due to the high frequency, the distances of the sensors can be

56 small, which enabled a very compact design. Overall material costs are specified
57 to be approximately 400 US-\$ (Wang et al., 2016).

58 The CSS does not need regular cleaning as the working principle is based on
59 relative deviations, not absolute irradiance measurements. As experienced over
60 more than two years of active service, this user-friendly maintenance routine was
61 found to hold even in the harsh conditions of the desert of Tabernas (Almería,
62 Spain). Although not cleaned, the CSS data are checked daily, e.g. to detect
63 constantly shaded sensors due to bird excrements. Luckily, such an event did
64 not occur yet. Based on this differential approach, the CSS is able to determine
65 the motion vectors of cloud shadows, not directly the motion vectors of the
66 clouds. However, these vectors deviate only insignificantly (Fung et al., 2013).

67 *2.2. Software adaptations of the CSS*

68 During this comparison campaign, no hardware adjustments were conducted
69 on the CSS. Suggestions for hardware improvements are mentioned in the con-
70 clusion. However, the evaluation method of the CSS is scrutinized and adapted.
71 All comparisons to the shadow camera measurements will be conducted on the
72 CSS with and without these adaptations.

73 *Increasing the detection rate*

74 In the first step of the evaluation algorithm, the CSS filters its data and it
75 does not provide cloud speed measurements if certain criteria are not met. In
76 any case, however, the raw data is stored. The filtering as implemented in Fung
77 et al. (2013) and Wang et al. (2016) is based on a second order error metric
78 (presented in the following), which results in a low number of calculated cloud
79 motion vectors in relation to the total number of shading events.

80 The algorithm used for the cloud motion measurements itself and de-
81 scribed in Wang et al. (2016) is the *LCE - curve fitting algorithm*, which deter-
82 mines the maximum cross-correlation coefficient R_{ij} of each pair of signals and
83 records the associated time shift $\Delta t_{i,j}$ for the sensor pair consisting of sensor
84 i and j corresponding to this maximum cross-correlation. Due to the setup of

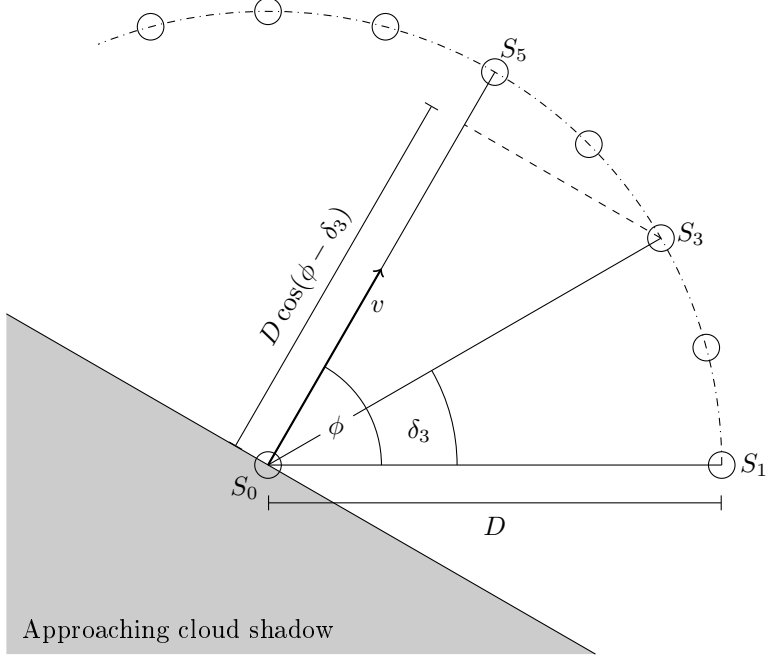


Figure 2: Depicted in the bottom-left corner is a shadow approaching the CSS with a speed v and a direction ϕ . Sensor S_0 is shaded first, sensor S_1 is shaded $\frac{D}{v} \cos(\phi)$ after S_0 . Then sensor S_3 is shaded $\frac{D}{v} \cos(\phi - \delta_3)$ and S_5 $\frac{D}{v}$ after S_0 . Based on these time differences, the motion vector of the shadow can be calculated.

85 the CSS, there are $\#(i \circ j) = \#\alpha = 12$ sensor pairs. Based on the time shifts of
 86 these sensor pairs, the speed is calculated. The method will be briefly described
 87 here and is explained in detail in Wang et al. (2016).

88 In Fig. 2, an example situation is shown. Coming from the bottom-left, a
 89 shadow is sequentially shading the sensors. The trigonometric relation visualized
 90 in Fig. 2 holds for all cloud edge directions as the cloud speed is assumed to be
 91 perpendicular to the cloud edge. Deviations caused by this this assumption are
 92 studied in section A.

93 The residuum of the cosine fit Γ acts as a filter (equ. 1).

$$94 \quad \Gamma = 1 - \frac{\sum_{\alpha=1}^{12} (t_{\alpha, Fit}(\phi, v) - t_{\alpha})^2}{t_{RMS}} \quad (1)$$

95 It is calculated with $t_{\alpha,Fit}(\phi, v)$ being the time shift according to the calculated
 96 cosine fit, t_{α} being the measured time shift and t_{RMS} being the quadratic scatter
 97 of the time shifts according to equ. 2.

$$98 \quad t_{RMS} = \sum_{\alpha=1}^{12} (t_{\alpha} - \frac{1}{12} \sum_{\alpha=1}^{12} t_{\alpha})^2 \quad (2)$$

99 If the average of the maximum cross-correlation coefficients R_{ij} is less than 0.9
 100 or the residuum Γ of the cosine curve fit is less than 0.9, the cloud motion
 101 vector will not be computed. A small R_{ij} is likely a result of an erroneous
 102 measurement or dynamically changing clouds. Similar, a small Γ indicates poor
 103 curve fitting and therefore an unreliable result. Based on these two criteria,
 104 measurements are rejected. The calculation of the cosine fit is based on a least
 105 square approach (LSQ). This approach, presented in Wang et al. (2016), is
 106 highly sensitive towards outliers and thus rejects many measurements.

107 In order to reduce the influence of outliers towards the cosine fit, several
 108 regression models such as the least square method (LSQ, Wang et al. (2016)), the
 109 *least absolute deviation method* (LAD, Bloomfield and Steiger (2012)), the *least*
 110 *trimmed squares method* (LTS, Giloni and Padberg (2002), Mount et al. (2014))
 111 and the *least median of squares method* (LMS, Rousseeuw (1984)) were studied.
 112 All methods are discussed in detail in the literature (Rousseeuw and Croux
 113 (1993), Huber (2009)) and will not be introduced here. Considering 347023
 114 measuring intervals on 223 days, the LSQ method obtains 5830 cloud motion
 115 vectors (speed and direction). The LAD method obtains 8034, the LTS method
 116 17334 and the LMS method 21535 motion vectors. The LTS method is found
 117 to have the least deviations in comparison to the LSQ method and yields 197 %
 118 more measurements on 223 days (91 % more measurements on the 59 days which
 119 could be temporally matched to shadow camera measurements as considered in
 120 section 4.2 and section 4.3). The CSS measurements derived from both the
 121 LSQ and the LTS method will be compared to shadow camera measurements.
 122 In section 4.4, the determination of the detection rate is presented.

123 Lowering the thresholds of the LSQ method can also be used to obtain more
 124 measurements. However, these additional measurements are far less accurate if



Figure 3: One of the six shadow cameras overlooking the PSA from top of a tower (CIEMAT CESA-I), 87 m above the ground.

125 compared to the shadow camera measurements.

126 **3. The shadow camera reference**

127 The shadow camera measures cloud motion vectors (speeds and directions)
128 by comparing three concurrent images. It is based on one off-the-shelf surveil-
129 lance camera (Mobotix MX-M24M-Sec-D22, CMOS sensor) and located on a
130 87 m high tower (CIEMAT CESA-I, Fig. 3 displays a shadow camera). Ev-
131 ery 15 s, an 8 bit RGB image of 2048×1536 pixels is taken (Fig. 4a). Using
132 both the determined interior (using methods described in Scaramuzza et al.
133 (2006)) and external (via GPS reference points) orientation, an orthoimage is
134 calculated (Fig. 4b). In this orthoimage, the dimensions of all pixels are known

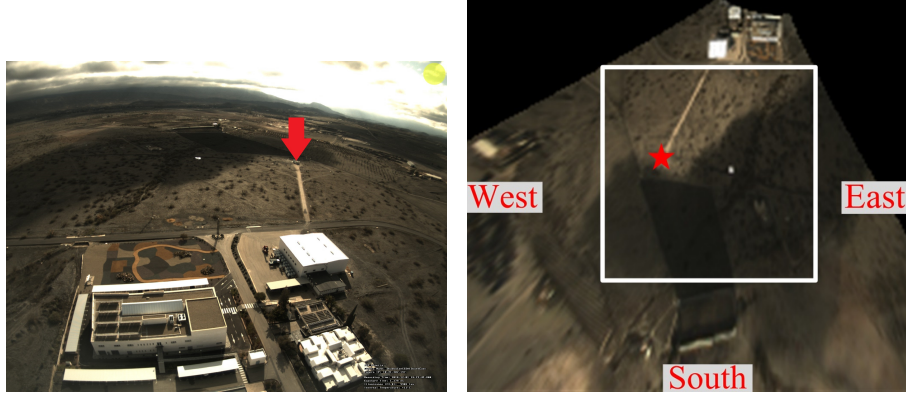


Figure 4: Left: raw image of the used shadow camera. The arrow marks the position of the CSS. Right: undistorted raw image as projected on a ground model. The star marks the position of the CSS. The white frame depicts the $525 \text{ m} \times 525 \text{ m}$ large area in which cloud shadow speeds are determined.

135 in [m]. From three concurrent orthoimages and a novel differential approach,
 136 cloud speeds and cloud directions are resolved. Due to the viewing geometry,
 137 pixels imaging areas far away from the camera's position are distorted (see e.g.
 138 bottom-left in Fig. 4b). In order to derive robust cloud motion vectors, only a
 139 quadratic area of 105×105 pixels ($525 \text{ m} \times 525 \text{ m}$) within the orthoimage is
 140 considered.

141 The approach to derive cloud (shadow) motion vectors is visualized in Fig. 5.
 142 Three subsequent cropped orthoimages corresponding to the timestamps t , $t - \Delta t$
 143 and $t - 2\Delta t$ are converted to grayscale and two difference images d_i are derived.
 144 The first difference image d_1 is the absolute of the subtraction of the image t and
 145 image $t - \Delta t$. The second difference image d_2 is the absolute of the subtraction
 146 of the images $t - \Delta t$ and $t - 2\Delta t$. The approach is given in equ. 3 and equ. 4
 147 with Δt being 15 s. x and y are the pixel coordinates in the cropped grayscale
 148 orthoimages im_{ortho} .

$$149 \quad d_1(x, y) = im_{ortho}(x, y, t) - im_{ortho}(x, y, t - \Delta t) \quad (3)$$

$$150 \quad d_2(x, y) = im_{ortho}(x, y, t - \Delta t) - im_{ortho}(x, y, t - 2\Delta t) \quad (4)$$

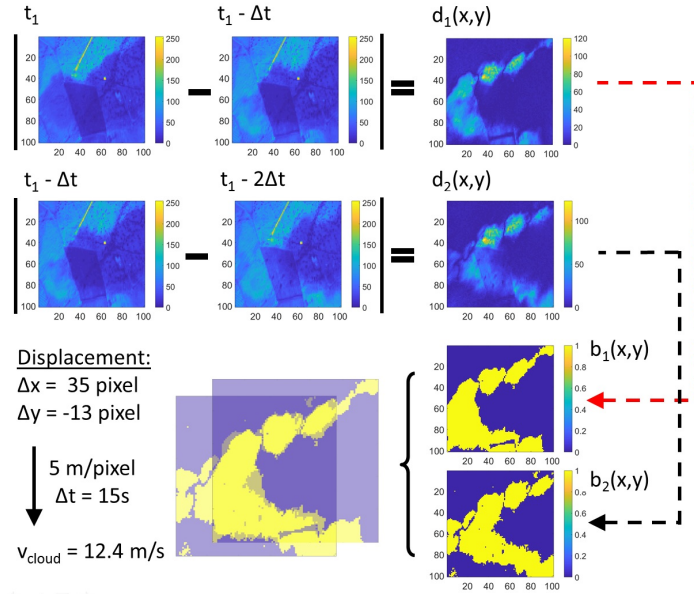


Figure 5: Shadow camera deriving cloud motion vectors: from three subsequent cropped and grayscale-converted orthoimages, difference images d_i are calculated. Via an empirically found threshold, binary difference images b_i are derived. These two difference images are then matched using cross-correlation. For the example situation depicted here (2016-12-01, 14:15:15 h - 14:15:45 h, UTC+1), a displacement of $\Delta x = 35$ pixel and $\Delta y = -13$ pixel is calculated. This corresponds to a shadow velocity of 12.4 m/s.

152 The difference images are converted into binary images b_i by an empirically
 153 found threshold (dashed arrows in Fig. 5). The pixel displacements Δx and Δy
 154 between the two binary difference images b_i is obtained by the normalized 2-D
 155 cross-correlation approach presented in Huang et al. (2012) (see Fig. 5, bottom
 156 row). From the displacement vector, the cloud shadow speed can be derived
 157 using equ. 5.

$$158 \quad v = \frac{\sqrt{(\Delta x)^2 + (\Delta y)^2}}{\Delta t} \times k_{SC} \quad (5)$$

159 Caused by technical limitations, the shadow camera can reliably resolve
 160 cloud motion vectors up to 17.5 m/s. The limiting factor is a result of the
 161 temporal resolution of $\Delta t = 15$ s. This image acquisition rate is chosen to limit
 162 the amount of produced data. The camera itself can take up to 25 images per

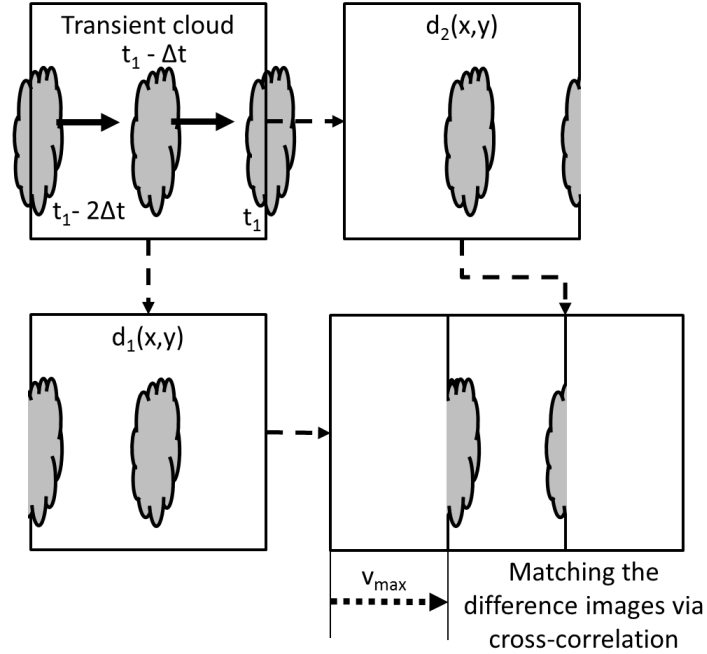


Figure 6: Visualization of the maximum resolvable velocity v_{max} : due to storage limitations, imposing a low image acquisition rate, the used shadow camera can reliably resolve cloud motion vectors up to 17.5 m/s.

163 second. The maximum velocity is calculated with equ. 6 and visualized in Fig. 6.

164

$$165 \quad v_{max} = \frac{Nk_{SC}}{2\Delta t} = 17.5 \text{ m/s} \quad (6)$$

166 Equation 6 is derived by looking at a cloud crossing the area under consideration
 167 in parallel to its borders (see Fig. 6). The quadratic imaged area has edge lengths
 168 of $Nk_{SC} = 105 \text{ pixel} \cdot 5 \text{ m/pixel} = 525 \text{ m}$. A cloud entering the imaged area
 169 at time $t - 2\Delta t$ and leaving it at time t results in a first (absolute) difference
 170 image d_1 with detected movements at a border and in the center. Similarly, the
 171 second difference image d_2 detects movements in the center and at the adjacent
 172 border. The matching via cross-correlation effectively divides the area by two,
 173 which this way defines the maximum resolvable velocity v_{max} .

174 The effects of this limitation will be discussed in section 4. In order to

175 detect cloud (shadow) movements, the shadow camera needs an reasonably ho-
 176 mogeneously area with little non-cloud movements and an elevated position for
 177 feasible viewing geometries. In Kuhn et al. (2018b), a system consisting of a
 178 shadow camera and an all-sky imager for cloud height determinations is pre-
 179 sented. Further applications of shadow cameras are discussed in Kuhn et al.
 180 (2017b).

181 To investigate the cloud motion vectors, each CSS measurement, without
 182 any temporal averaging, is compared to the ± 2 min (four-minute) median of the
 183 shadow camera measurements. Furthermore, ± 2 min (four-minute) and ± 5 min
 184 (ten-minute) medians of the CSS measurements are compared to corresponding
 185 shadow camera measurements. If within the individual temporal interval no
 186 reference measurement is available, the corresponding CSS measurements are
 187 dropped. As the shadow camera approach derives reliably velocities only up
 188 to 17.5 m/s, CSS measurements with a corresponding reference value above
 189 this speed are also dropped. For the investigation of cloud motion directions,
 190 vectors measured by the CSS and the shadow camera are compared to each
 191 other. Without the temporal averaging, the LSQ method is studied on 2956
 192 measurements and the LTS method on 4828 measurements for which shadow
 193 camera reference measurements are available. In total, the LSQ method derived
 194 3170 measurements on 59 days, the LTS method 6041 and the shadow camera
 195 23155. To quantify the deviations, root-mean-square deviations (RMSD), mean-
 196 absolute deviations (MAD) and the bias are calculated (equ. 7-9).

$$197 \quad \text{RMSD} = \sqrt{\frac{1}{N} \sum_{i=1}^N (v_{CSS,i} - v_{SC,i})^2} \quad (7)$$

$$198 \quad \text{MAD} = \frac{1}{N} \sum_{i=1}^N |v_{CSS,i} - v_{SC,i}| \quad (8)$$

$$199 \quad \text{bias} = \frac{1}{N} \sum_{i=1}^N (v_{CSS,i} - v_{SC,i}) \quad (9)$$

202 4. Benchmarking the CSS

203 In section 2.2, an algorithmic change in the software of the CSS is discussed,
204 which significantly increases the amount of detected shading events. In this
205 section, both approaches (LSQ and LTS, see section 2.2) are compared to the
206 shadow camera reference measurements. To begin with, three example days are
207 studied in detail in section 4.1. In section 4.2, cloud shadow speed measurements
208 are studied on 59 days. The directions of the cloud shadows are compared to
209 shadow camera measurements in section 4.3. The detection rate of the CSS is
210 investigated based on its radiometer measurements on 223 days in section 4.4
211 (not in comparison to the shadow camera). After focussing on the deviations
212 found with the LSQ approach, the deviations of the LTS approach, yielding
213 more measurements, are discussed in section 4.5.

214 The speed distributions as measured by the CSS and the shadow camera is
215 depicted in Fig. 7. In the top left, the overall number of occurrence is shown.
216 The shadow camera obtains far more measurements than the CSS, for which
217 the LTS method yields more results than the LSQ method. The vertical line
218 marks the maximum speed reliably resolvable by the shadow camera (17.5 m/s,
219 see section 3). This limit was derived for a worst case scenario. Cloud shad-
220 ows moving diagonally over the imaged area can be reliably measured up to
221 $17.5 \text{ m/s} \cdot \sqrt{2} = 24.7 \text{ m/s}$. In extreme cases, diagonal cloud shadow speeds up
222 to $525 \text{ m/15 s} \cdot \sqrt{2} = 49.5 \text{ m/s}$ can be measured. However, beyond 17.5 m/s,
223 the speeds cannot be safely resolved for all directions. 92.6 % of all shadow
224 camera measurements are below 24.7 m/s, 81.4 % of all shadow camera mea-
225 surements are below 17.5 m/s. 92.1 % of all CSS measurements obtained with
226 the LSQ method are below 17.5 m/s (98.5 % below 24.7 m/s). 93.0 % of all
227 CSS measurements derived with the LTS method are below 17.5 m/s (98.1 %
228 below 24.7 m/s). Given the distribution of the speeds measured by the CSS
229 and the limitations of the shadow camera, all shadow camera measurements
230 beyond 17.5 m/s are excluded from the comparisons in this section. For speeds
231 considered in the following comparisons ($v \leq 17.5 \text{ m/s}$), the mean speed of

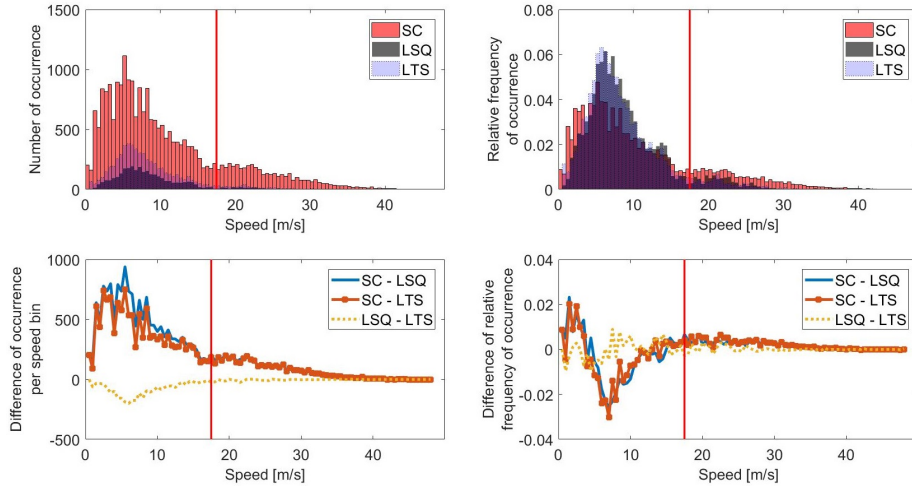


Figure 7: Top left: histograms of all cloud motion vectors obtained on 59 days by the shadow camera (SC), the CSS using the LSQ method (LSQ) and the CSS using the LTS method (LTS). Top right: relative frequency of occurrence. Bottom left: bin-wise subtraction of the number of occurrence (see top left). Bottom right: bin-wise subtraction of the relative frequency of occurrence (see top right). The vertical line marks the maximum speed reliably resolvable by the shadow camera for all cloud motion directions.

232 the shadow camera measurements is 7.36 m/s (median: 6.67 m/s), the mean
 233 speed of the CSS measurements with the LSQ approach is 8.99 m/s (median:
 234 7.69 m/s) and with the LTS approach 8.60 m/s (median: 7.30 m/s). Although
 235 the modes of the histograms are at 6.0 m/s, a wide range of cloud speeds are
 236 measured.

237 4.1. Three example days

238 Before looking at long-term comparisons in the next sections, three example
 239 days are specifically studied. The example days are 2016-03-19, 2016-04-22
 240 and 2016-10-14. For these example days, the CSS data are shown without any
 241 temporal averaging. The effects of temporal averaging on the comparisons are
 242 studied in the next sections.

243 The cloud speeds and direction of 2016-10-14 are shown in Fig. 9. Cloud mo-
 244 tion directions are displayed in the top part, cloud velocities in the bottom part.

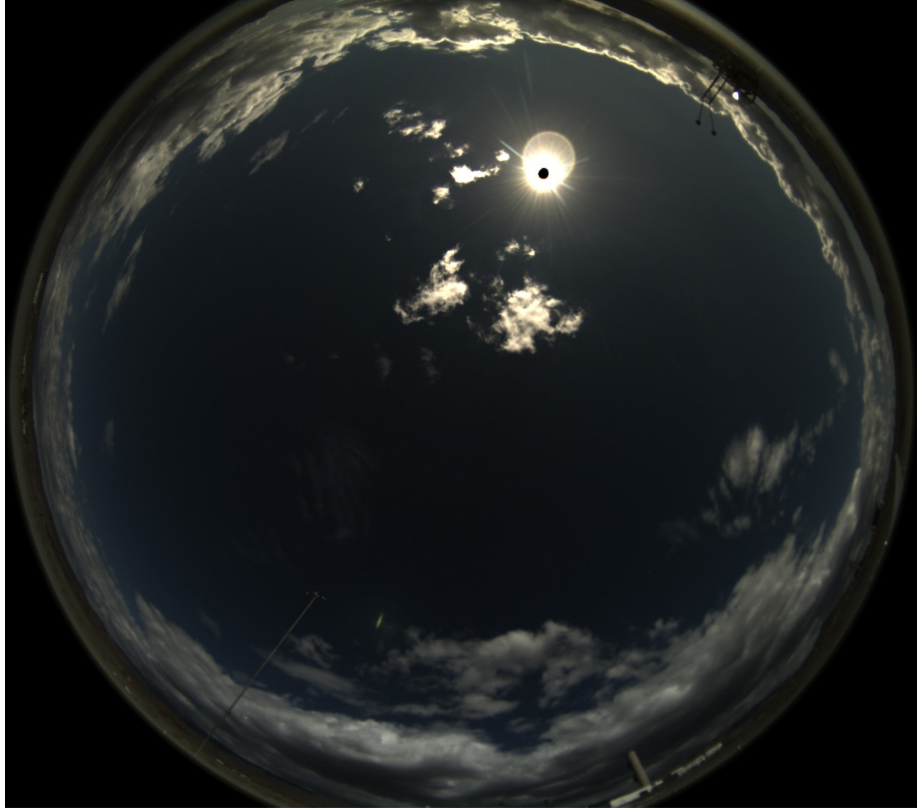


Figure 8: All-sky image taken at 2016-10-14, 12:10:00 UTC+1. Small clouds are visible around the sun, which are dynamically forming.

245 The values of the reference system are depicted as ± 2 min medians; the CSS
246 measurements are not additionally averaged or filtered. On this day, altocumu-
247 lus clouds between 2000 and 3000 m are predominant, traveling from north-west
248 to south-east. The shadow camera obtained 653 measurements on this day, the
249 CSS with the LSQ method 60 and with the LTS method 111 measurements.

250 Prior to 12:31 h (UTC+1), the shadow camera does not provide measure-
251 ments. Looking at the shadow camera video of this day, the lack of measure-
252 ments can be explained by a lack of (visible) shading events. The shading events
253 measured by the CSS are not visible in the shadow camera video. However, the
254 data of a near-by all-sky imager show that around 12:15 h there are some tiny

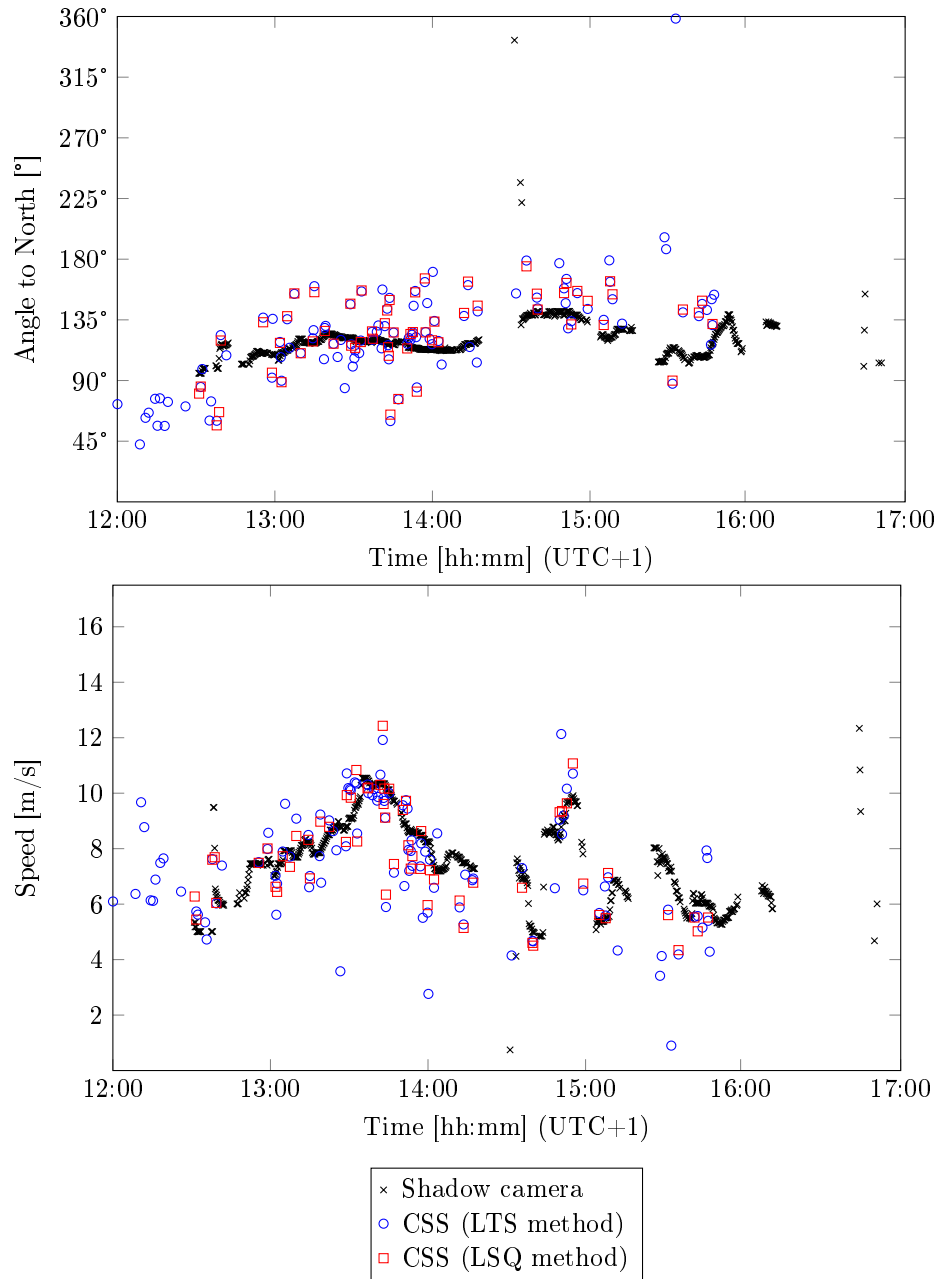


Figure 9: CSS and shadow camera measurements on 2016-10-14. The shadow camera reference measurements show less scatter than the CSS measurements.

255 clouds dynamically forming around the sun (see Fig. 8). This might be an ex-
 256 ample of a nugget effect with the spatial resolution of the CSS being far higher
 257 than the spatial resolution of the shadow camera at the position of the CSS.
 258 This effect and its impact on these comparisons are discussed later and partially
 259 compensated by temporal averaging later-on.

260 Between 12:30 h (UTC+1) and 14:30 h, the measured velocities increase from
 261 approximately 5 m/s to 10 m/s and decrease back to approximately 6 m/s. Later
 262 that day, large scattered clouds with different velocities are present. For this
 263 day, the CSS measurements and the reference system align very well. Ceilometer
 264 data and all-sky imager videos show that there is only one cloud layer present.
 265 The deviation found on this day for the LSQ and the LTS method are displayed
 in Tab. 1.

Table 1: Deviations between the LSQ and LTS approach in comparison to the shadow camera on 2016-10-14. Instantaneous CSS measurements without any temporal averaging are compared to ± 2 min medians derived from the shadow camera. The deviations of the cloud motion direction are calculated from vectors.

| | LSQ approach | LTS approach |
|------|----------------|-----------------|
| RMSD | 1.1 m/s, 25.6° | 1.6 m/s, 28.4° |
| MAD | 0.8 m/s, 20.3° | 1.1 m/s, 21.0° |
| bias | -0.2 m/s, 8.3° | -0.4 m/s, 10.1° |

266

267 Figure 10 visualizes cloud shadow speeds on 2016-03-19 as measured by the
 268 shadow camera and calculated by the two algorithmic approaches derived from
 269 CSS measurements.

270 There is one dominant cloud direction (from west to east) throughout the
 271 day, both for the shadow camera and the CSS. However, there is variation in
 272 cloud speed due to clouds at different heights, as suggested by ceilometer and
 273 all-sky imager data (not shown). In general, there is much scatter and large
 274 deviations between the measurements. This is partially caused by multiple cloud
 275 layers present on this day, which pose a challenge both for the shadow camera
 276 and the CSS. Moreover, for the CSS, optically thin clouds are challenging. Their

277 diffuse edges often do not trigger CSS measurements or only measurements with
 278 low accuracy. The detection rates of the CSS for 12 shading classes are discussed
 279 in section 4.4.

280 Optically thin clouds are found to be less critical for the shadow camera
 281 system. Mixed situations with both optically thin and thick clouds present pose
 282 a challenge for the shadow camera system. However, such mixed situations are
 283 not predominant on the area imaged by the shadow camera.

284 Between 14:00 h and 14:30 h, a thick cloud is blocking the sun in the whole
 285 area image by the shadow camera. The shadow camera is not able to derive
 286 measurements out of this very dark shadow.

287 Applying the methodology described in section 4.2, the deviations found on
 this day for the LSQ and the LTS method are displayed in Tab. 2.

Table 2: Deviations found for the LSQ and LTS approach in comparison to the shadow camera on 2016-03-19. Instantaneous CSS measurements without any temporal averaging are compared to ± 2 min medians derived from the shadow camera.

| | LSQ approach | LTS approach |
|------|----------------|----------------|
| RMSD | 2.7 m/s, 31.4° | 3.9 m/s, 39.5° |
| MAD | 1.8 m/s, 23.1° | 2.7 m/s, 29.9° |
| bias | -0.7 m/s, 8.3° | -1.6 m/s, 9.5° |

288

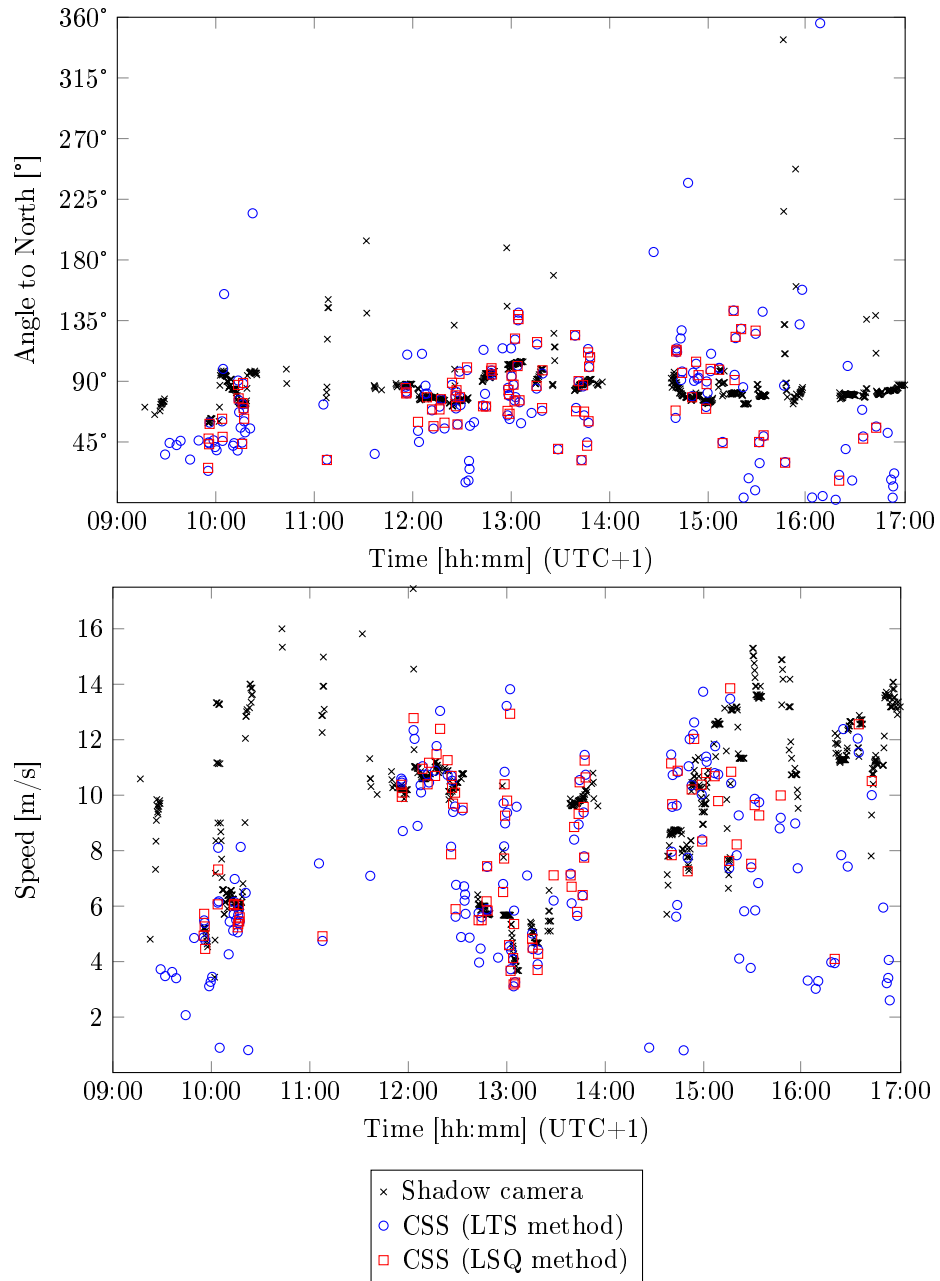


Figure 10: CSS and shadow camera measurements on 2016-03-19. Due to multiple cloud layers and optically thin clouds, both scatter and significant deviations between the CSS measurements and the shadow camera reference systems are present.

289 The cloud speeds and direction of 2016-04-22 are depicted in Fig. 11. On
 290 this day, mainly altocumulus clouds with an altitude of 2000 m are present.
 291 Both the measured cloud directions and the measured cloud speeds are not
 292 homogeneous throughout the day. Between 11:00 h (UTC+1) and 12:30 h, the
 293 CSS measurements scatter strongly in comparison to the reference system. Also,
 294 a bias in the velocities is found. The origins of these deviations lay in a key
 295 assumption of the linear cloud edge - curve fitting method, which is discussed in
 296 appendix A. Between 13:00 h (UTC+1) and 15:00 h, there is a high correlation
 297 between the measurements.

298 Between 16:00 h (UTC+1) and 16:30 h, the CSS is shaded by clouds, but
 299 does not provide any measurements. Looking at all-sky and shadow camera
 300 images as well as ceilometer data reveals that this is caused by optically thin
 301 clouds with diffuse edges at approximately 4000 m altitude. Their speed is
 302 beyond the limits of the reference system (17.5 m/s).

303 After 16:30 h (UTC+1), there is a significant amount of scatter. All-sky
 304 imager data testify multiple cloud layers during this time. The deviation found
 on this day for the LSQ and the LTS method are displayed in Tab. 3.

Table 3: Deviations found for the LSQ and LTS approach in comparison to the shadow camera on 2016-04-22. Instantaneous CSS measurements without any temporal averaging are compared to ± 2 min medians derived from the shadow camera.

| | LSQ approach | LTS approach |
|------|----------------|----------------|
| RMSD | 1.6 m/s, 24.9° | 1.9 m/s, 37.8° |
| MAD | 1.2 m/s, 20.1° | 1.4 m/s, 25.6° |
| bias | -0.8 m/s, 3.9° | -0.8 m/s, 1.3° |

305

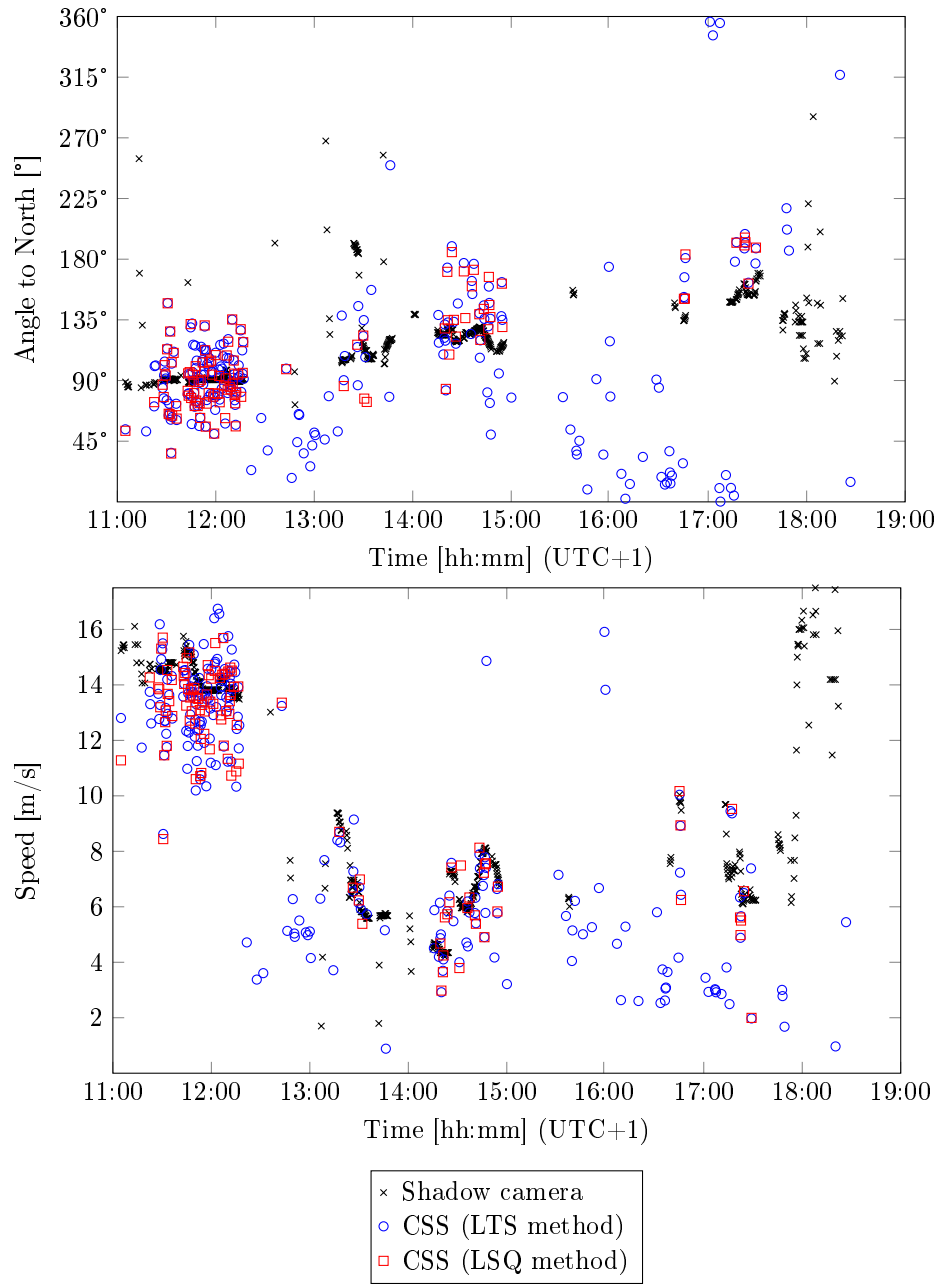


Figure 11: CSS and shadow camera measurements on 2016-04-22. Both the cloud directions and the cloud speeds change multiple times during the day.

306 *4.2. Comparing cloud shadow speeds: CSS against shadow camera*

307 During the comparison period of 59 days, the CSS obtained 3170 cloud
 308 motions vectors with the LSQ approach (for details see section 2.2). The shadow
 309 camera measured 23155 cloud motion vectors. This discrepancy between the
 310 amount of CSS measurements and the shadow camera approach is partially
 311 caused by optically thin clouds, which often do not trigger a CSS measurement
 312 (see section 4.4), and by the area of the measurements. The CSS is statistically
 313 not shaded as often as the area imaged by the reference system because these
 314 two areas have far different sizes (CSS: approximately 0.09 m²; shadow camera:
 315 approximately 0.28 km²).

316 The deviations found for the LSQ method in comparison to the shadow
 317 camera measurements are displayed in Tab. 4 without any temporal averaging,
 318 ± 2 min medians ($\overline{\text{LSQ}}_{\pm 2 \text{ min}}$) and ± 5 min temporal medians ($\overline{\text{LSQ}}_{\pm 5 \text{ min}}$).

319 The deviations are visualized in a scatter density plot in Fig. 12. The de-
 320 viations stem mostly from optically thin clouds and clouds at large altitudes
 321 (see Kuhn et al. (2018b)). If such clouds trigger CSS measurements at all, the
 322 accuracy is poor.

Table 4: Deviations found for the LSQ approach for measurements with and without temporal averaging in comparison to the shadow camera measurements on 59 days (shadow speed).

| | LSQ approach | $\overline{\text{LSQ}}_{\pm 2 \text{ min}}$ | $\overline{\text{LSQ}}_{\pm 5 \text{ min}}$ |
|------|------------------|---|---|
| RMSD | 2.7 m/s (36.6 %) | 2.4 m/s (32.7 %) | 2.1 m/s (28.0 %) |
| MAD | 1.6 m/s (21.9 %) | 1.3 m/s (18.0 %) | 1.2 m/s (15.7 %) |
| bias | -0.2 m/s (2.7 %) | -0.2 m/s (2.5 %) | -0.2 m/s (2.8 %) |

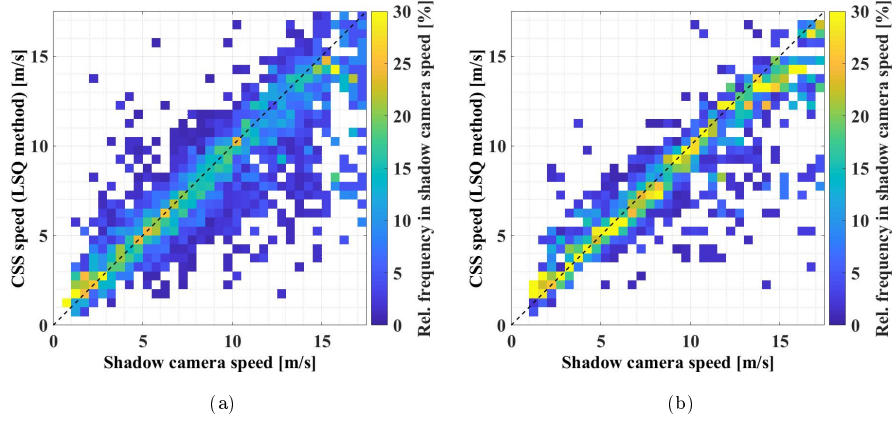


Figure 12: Scatter density plots of the speeds measured by the CSS and the shadow camera. Figure 12a: LSQ method without temporal averaging, Fig. 12b: LSQ method with ± 5 min temporal medians. The colorbar represents the relative frequency of a given pixel within the corresponding shadow camera speed bin. Each column adds up to 100 %. In total, the LSQ method obtained 3170 measurements of which 2956 could be temporally matched to shadow camera measurements.

323 4.3. Comparing cloud shadow directions: CSS against shadow camera

324 This section compares the cloud shadow directions as measured by the CSS
 325 against the reference shadow camera. The data set for this comparison is the
 326 same as in section 4.2. The deviations found for the LSQ method in compar-
 327 ison to the shadow camera regarding the shadow directions are displayed in
 328 Tab. 5. Although there is only a minor bias present, the deviations do not
 329 shrink significantly with larger temporal medians. This is an indication that
 330 systematic offsets are present between the CSS and the shadow camera mea-
 331 surements. These offsets can be explained by the different area from which these
 332 two systems derive their cloud motion vectors. For the shadow camera, this is
 333 a relatively large area. Therefore, the obtained cloud motion direction is an
 334 average direction. The CSS, however, might be able to resolve smaller cloud
 335 movements, e.g. rotations or very small clouds (such as the clouds at 12:15 h,
 336 2016-10-14, as discussed in section 4.1). Furthermore, the CSS measurements
 337 are based on the assumptions of the linear cloud edge - curve fitting method,

Table 5: Deviations found for the LSQ approach in comparison to the shadow camera approach on 59 days with and without temporal averaging (shadow motion direction, $180^\circ=100\%$).

| | LSQ approach | $\overline{\text{LSQ}}_{\pm 2 \text{ min}}$ | $\overline{\text{LSQ}}_{\pm 5 \text{ min}}$ |
|------|----------------|---|---|
| RMSD | 50.2° (28.0 %) | 52.2° (29.0 %) | 47.9° (26.6 %) |
| MAD | 30.4° (16,8 %) | 28.2° (15.6 %) | 25.3° (14.0 %) |
| bias | 0.5° (0.2 %) | 3.4° (2.0 %) | 3.7° (2.0 %) |

338 which is visualized in Fig. 2 and discussed in appendix A. If e.g. a cloud shades
 339 the CSS with a saw tooth edge of suitable size, the measured direction might
 340 not be the general direction of the cloud. Such systematic offsets could explain
 341 the behavior seen in Tab. 5 as well as the scatter seen in Fig. 13.

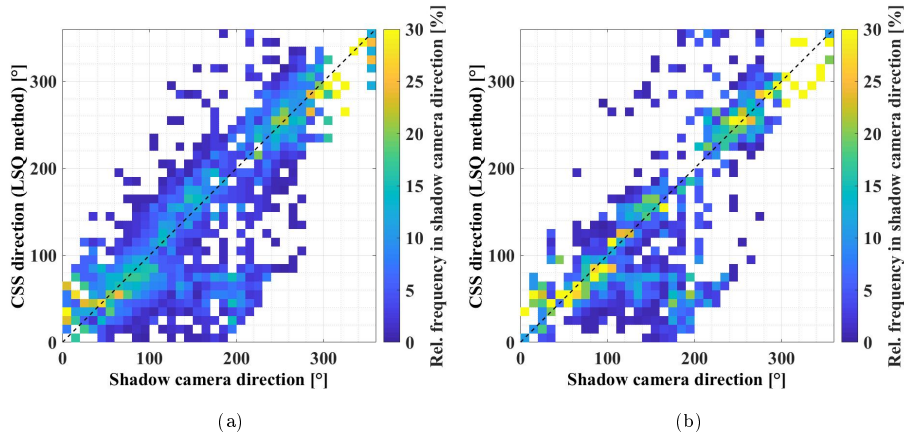


Figure 13: Scatter density plot of CSS LSQ without temporal averaging (a) and CSS LSQ with ± 5 min temporal medians (b) cloud directions versus the shadow camera cloud directions. The colorbar represents the relative frequency of a given pixel within the corresponding shadow camera direction bin.

342 4.4. Investigating the detection rate of the CSS

343 In section 2.2, a method to increase the detection rate of the CSS is discussed.
 344 The validation presented in this section is conducted on 223 days (from 2016-
 345 03-20 to 2016-10-28). The validation of the detection rate is not conducted in

346 comparison to the shadow camera, but in comparison to normalized irradiance
 347 measurements of the CSS itself. This approach is chosen to avoid scale effects
 348 between the shadow camera and the CSS. These scale effects are clouds seen by
 349 the CSS but not by the shadow camera, clouds imaged by the shadow camera
 350 but not shading the CSS and shadows beyond the temporal resolution of one
 351 system. The approach to investigate the detection rate of the CSS by looking
 352 at the CSS raw data is described in the following.

Figure 14 displays an example day as measured by one of the nine CSS sen-
 sors. A clear sky global horizontal irradiance (CSF) model described in Han-
 rieder et al. (2016) is added and the sensor signals are calibrated to the mea-
 surements of a close-by GHI reference station. Furthermore, the 9 s missing
 data after each 9 s measurement are linearly interpolated. Using a clear sky

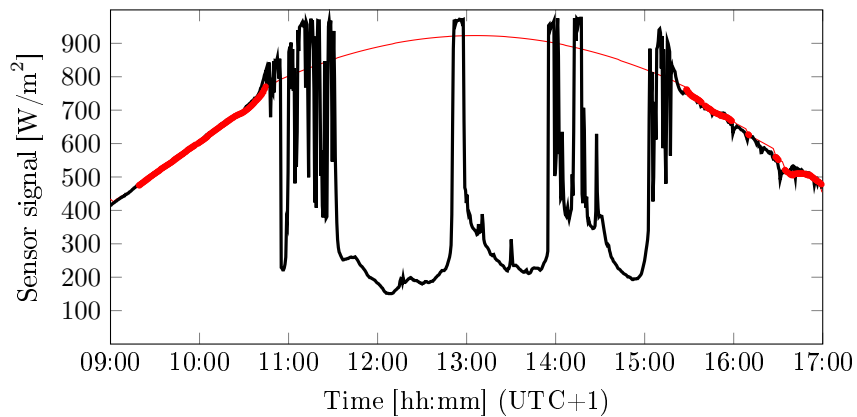


Figure 14: Example day with added clear sky reference (2016-08-25). DHI overshootings and shading events caused by transient clouds are visible.

modeling (CSM), shading strengths (SS) can be defined (Mäki and Valkealahti, 2012):

$$SS = \frac{GHI^{CSM} - GHI}{GHI^{CSM}} \quad (10)$$

353 In equation 10, GHI is the measured and calibrated irradiance from one of the
 354 9 CSS sensors and GHI^{CSM} is the modeled clear sky irradiance. Calibration is
 355 performed using another calibrated reference pyranometer approximately 500 m

356 away from the CSS and a dynamic adaption factor for the CSS sensor signal.
357 The deviations from the modeled clear sky irradiance are used to determine the
358 amount of shading events detected by the CSS. A shading event begins after
359 the ratio of the measured GHI and the clear sky GHI falls below 90 % and ends
360 if it is again above this threshold. The shading strength is derived from the
361 minimum measured GHI between these two timestamps.

362 All shadings are characterized into 12 classes by their shadings strengths and
363 shading duration. Shading strengths are divided into three different classes:

- 364 • ≤ 30 % for optically thinner clouds
- 365 • > 30 % and ≤ 60 % for thicker thin clouds
- 366 • > 60 % for optically thicker clouds

367 Shading durations are resolved into four classes:

- 368 • ≤ 60 s for short shading durations
- 369 • > 60 s and ≤ 300 s for medium shading durations
- 370 • > 300 s and ≤ 600 s for long shading durations
- 371 • > 600 s for (partial) overcast situations

372 The relative share of each class as measured from 2016-03-20 to 2016-10-28
373 (223 days) is shown in Tab. 6. Predominantly, there are optically thin clouds
374 with short shading durations above the PSA.

Table 6: Classifications based on shading strength and shading duration: Amount of events per class from 2016-03-20 to 2016-10-28 (223 days). Optically thin clouds with short shading durations are most common. Total amount of shading events (per sensor): 8276.

| | | Shading duration [s] | | | | <i>sum</i> |
|------------------|-----------|----------------------|----------|-----------|-------|------------|
| | | < 60 | 60 – 300 | 300 – 600 | > 600 | |
| Shading strength | > 60 % | 3.4 % | 3.8 % | 0.9 % | 2.4 % | 10.5 % |
| | 30 – 60 % | 18.3 % | 8.4 % | 1.8 % | 1.9 % | 30.4 % |
| | < 30 % | 52.9 % | 5.3 % | 0.7 % | 0.3 % | 59.1 % |
| <i>sum</i> | | 74.6 % | 17.4 % | 3.4 % | 4.6 % | |

375 In Tab. 7, the detected CSS measurements per shading class are depicted
376 using the LSQ approach. The CSS measures only 4.8 % of optically thin clouds
377 with shading durations above 600 s and is best for optically thick clouds with
378 short shading durations (21.6 % detected events). The rate of successfully de-
379 tected shading events is low.

380 Using the LSQ approach (see section 2.2) 5830 shading events are detected
381 between 2016-03-20 and 2016-10-28 (223 days).

Table 7: Detection rates for each shading class: Relative share of shading events detected by the CSS using the LSQ algorithm from 2016-03-20 to 2016-10-28 (223 days). Total amount of detected shading events: 8276.

| | | Shading duration [s] | | | |
|------------------|-----------|----------------------|----------|-----------|-------|
| | | < 60 | 60 – 300 | 300 – 600 | > 600 |
| Shading strength | > 60 % | 21.6 % | 16.4 % | 16.7 % | 9.5 % |
| | 30 – 60 % | 16.0 % | 13.7 % | 9.5 % | 6.3 % |
| | < 30 % | 8.0 % | 3.7 % | 3.7 % | 4.8 % |

382 4.5. Comparing CSS software approaches: LSQ and LTS

383 In section 2.2, the methodology used by the CSS to derive cloud motion
 384 vectors is presented and ways to increase the detection rate are discussed. As
 385 can be seen in section 4.4, the detection rate is low. This can be improved
 386 by using the LTS approach instead of the LSQ approach. In this section, the
 387 deviations found in comparison to the shadow camera using the CSS with the
 388 LTS approach are investigated. Moreover, these deviations are compared to the
 389 deviations obtained with the CSS and the LSQ approach.

390 In comparison to the histogram found for the LSQ approach (see Fig. 7), no
 391 significant deviations are present. During the comparison period of 59 days, the
 392 CSS obtained 6041 cloud motion vectors using the LTS method (3170 for the
 393 LSQ approach, 23155 with the shadow camera).

394 The deviations found for the LSQ and LTS method in comparison to the
 395 shadow camera measurements are displayed in Tab. 8 without any temporal
 396 averaging, ± 2 min medians and ± 5 min medians. The LTS approach shows
 397 higher deviations in comparison to the shadow camera. However, for ± 5 min
 398 temporal medians (LSQ: 2705 temporally averaged measurements with corre-
 399 sponding shadow camera reference measurements, LTS: 4350 measurements),
 400 the deviations for both LSQ and LTS are similar.

401 In general, the measurements obtained by the LTS method are less accurate,
 402 but far more frequent in comparison to the LSQ method. This is also visualized
 403 in the scatter density plots in Fig. 15.

404 Table 9 investigates the origin of the larger deviations found using the LTS
 405 method. $LTS \in LSQ$ derives the deviations for all LTS measurements which are

Table 8: Deviations found for the LSQ and LTS approach for measurements with and without temporal averaging in comparison to the shadow camera measurements on 59 days (shadow speed).

| | LSQ approach | $\overline{LSQ}_{\pm 2 \text{ min}}$ | $\overline{LSQ}_{\pm 5 \text{ min}}$ | LTS approach | $\overline{LTS}_{\pm 2 \text{ min}}$ | $\overline{LTS}_{\pm 5 \text{ min}}$ |
|------|-------------------|--------------------------------------|--------------------------------------|-------------------|--------------------------------------|--------------------------------------|
| RMSD | 2.7 m/s (36.6 %) | 2.4 m/s (32.7 %) | 2.1 m/s (28.0 %) | 3.4 m/s (45.8 %) | 2.9 m/s (39.2 %) | 2.6 m/s (35.2 %) |
| MAD | 1.6 m/s (21.9 %) | 1.3 m/s (18.0 %) | 1.2 m/s (15.7 %) | 2.1 m/s (28.0 %) | 1.7 m/s (22.4 %) | 1.5 m/s (20.2 %) |
| bias | -0.2 m/s (-2.7 %) | -0.2 m/s (-2.5 %) | -0.2 m/s (-2.8 %) | -0.4 m/s (-5.8 %) | -0.4 m/s (-5.1 %) | -0.4 m/s (-5.7 %) |

Table 9: Deviations found for LTS approach adjacent and not adjacent to obtained LSQ measurements in comparison to the shadow camera measurements on 59 days (shadow speed).

| | LTS \in LSQ | $\overline{\text{LTS} \in \text{LSQ}}_{\pm 1 \text{ min}}$ | LTS \notin LSQ | $\overline{\text{LTS} \notin \text{LSQ}}_{\pm 1 \text{ min}}$ |
|------|-------------------|--|--------------------|---|
| RMSD | 2.9 m/s (39.0 %) | 2.4 m/s (32.0 %) | 5.4 m/s (73.2 %) | 5.2 m/s (70.6 %) |
| MAD | 1.8 m/s (24.2 %) | 1.4 m/s (19.3 %) | 3.7 m/s (49.7 %) | 3.5 m/s (47.2 %) |
| bias | -0.2 m/s (-3.0 %) | -0.2 m/s (-2.7 %) | -1.6 m/s (-21.2 %) | -1.6 m/s (-21.8 %) |

406 within ± 1 min around a LSQ measurement (3517, 84.8 %). $\overline{\text{LTS} \in \text{LSQ}}_{2 \text{ min}}$
407 compares these ± 1 min temporal medians to the shadow camera measurements.
408 LTS \notin LSQ calculates the deviations for LTS measurements, which are not
409 within ± 1 min around a LSQ measurement (630, 15.2 %). $\overline{\text{LTS} \notin \text{LSQ}}_{2 \text{ min}}$
410 derives the deviations for these measurements as medians over ± 1 min.

411 The measurements rejected by the LSQ approach but accepted by the LTS
412 method show far higher deviations in comparison to the shadow camera mea-
413 surements. Thus the LTS method, providing more measurements, shows similar
414 deviations for situations in which the LSQ method obtains measurements but
415 displays high deviations otherwise.

416 Figure 15b compares the velocities derived from the LSQ and LTS method
417 to each other by taking the ± 2 min median of the LSQ measurements around a
418 LTS measurement. No systematic bias is present and there is a high correlation.
419 The largest deviations occur for velocities above 15 m/s.

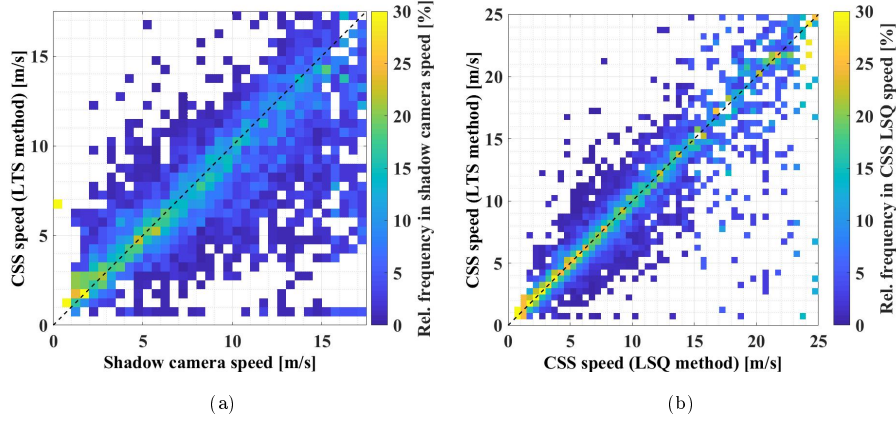


Figure 15: Scatter density plots of measured cloud speeds on 59 days. Figure 15a: LTS method (no temporal averaging, compare to Fig. 12), Fig. 15b: LSQ-LTS comparison. The colorbar represents the relative frequency of a given pixel within the corresponding shadow camera speed bin. Each column adds up to 100 %. In total, with the LSQ and LTS method, 3170 and 6041 measurements could be obtained, respectively. The shadow camera produced 23155 measurements.

420 The deviations found for the LSQ and LTS method in comparison to the
 421 shadow camera regarding the shadow directions are displayed in Tab. 4.5. Simi-
 422 lar to the deviations found for the velocities, the deviations for the LTS method
 423 are larger. However, more measurements are obtained with the LTS method
 424 in comparison to the LSQ method. As discussed for the direction deviations
 425 derived with the LSQ method (see section 4.3), temporal averaging does not
 426 reduce deviations as strongly as for the cloud velocities (compare with Tab. 8).
 427

Table 10: Deviations found for the LSQ and LTS approach in comparison to the shadow camera approach on 59 days with and without temporal averaging (shadow motion direction, $180^\circ = 100\%$).

| | LSQ approach | $\overline{\text{LSQ}}_{\pm 2 \text{ min}}$ | $\overline{\text{LSQ}}_{\pm 5 \text{ min}}$ | LTS approach | $\overline{\text{LTS}}_{\pm 2 \text{ min}}$ | $\overline{\text{LTS}}_{\pm 5 \text{ min}}$ |
|------|----------------|---|---|----------------|---|---|
| RMSD | 50.2° (28.0 %) | 52.2° (29.0 %) | 47.9° (26.6 %) | 58.4° (32.4 %) | 56.0° (30.8 %) | 55.2° (30.6 %) |
| MAD | 30.4° (16.8 %) | 28.2° (15.6 %) | 25.3° (14.0 %) | 35.7° (20.0 %) | 30.8° (17.2 %) | 30.0° (16.4 %) |
| bias | 0.5° (0.2 %) | 3.4° (2.0 %) | 3.7° (2.0 %) | 1.1° (0.6 %) | 3.0° (1.6 %) | 4.4° (2.4 %) |

428 In Fig. 16, the LTS derived cloud shadow directions without temporal aver-
 429 aging are compared to corresponding shadow camera measurements and mea-
 430 surements obtained from the CSS-LSQ approach. Although the measurements
 431 align, there is a significant amount of scatter.

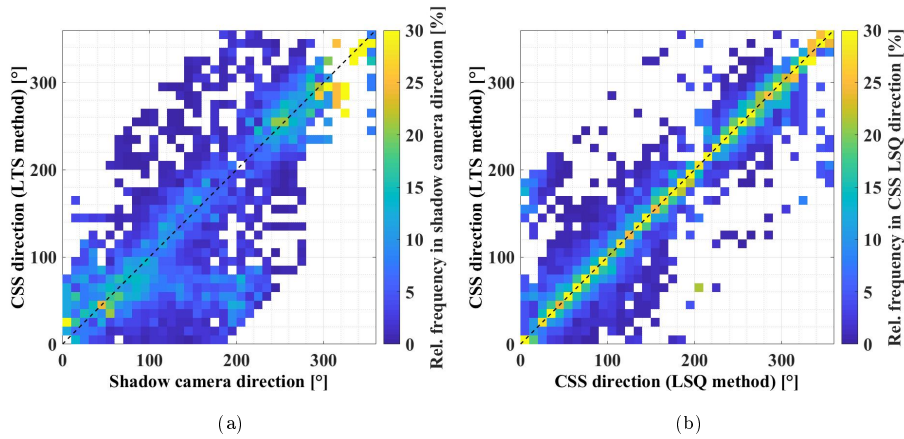


Figure 16: Scatter density plot of CSS LTS cloud directions without temporal medians versus the shadow camera cloud directions (a) and versus CSS LSQ cloud directions (b), both with temporal medians of ± 2 min.

432 Figure 16b compares the directions obtained from the CSS with the LSQ
 433 and LTS method using a scatter density plot. The approach is similar to the
 434 approach for Fig. 15b. Although there is scatter, the two methods provide
 435 similar cloud directions for temporally adjacent measurements (see Tab. 9).

436 As a conclusion, the LTS method obtains more measurements than the LSQ
 437 method. However, for LTS measurements not temporally adjacent to LSQ mea-
 438 surements, the deviations in comparison to the shadow camera are large. How-
 439 ever, for some applications (e.g. industrially used cloud height measurement
 440 systems) a less accurate measurement might be better than no measurement at
 441 all and the LTS method can provide this trade-off.

442 **5. Caveats, advantages and disadvantages of the CSS and the novel**
443 **shadow camera approach**

444 The shadow camera needs proper orientation, an elevated position and an
445 area with little non-cloud movements. Also, pixels imaging mirrors and other
446 reflective objects cannot be evaluated. Furthermore, evaluating pixels imaging
447 photovoltaic panels or larger vegetation (e.g. forests) is difficult. Although the
448 lack of a strongly elevated position can be overcome by using elevated structures
449 of lower height (e.g. 10 m) and a higher image acquisition frequency, such a
450 system would have a disadvantage due to the smaller imaged area. If needed,
451 this issue could be overcome using multiple cameras.

452 One major disadvantage of this particular shadow camera is the temporal
453 availability of historic images. If an image is taken only every 15 s, very fast
454 clouds will already have transitioned past the image area. Changing the tempo-
455 ral resolution to multiple images per second requires only a simple software ad-
456 justment in the camera, but the data storage requirements become prohibitive.
457 For instance, a camera taking 3 MP images every 15 s accumulates on one day
458 over 12 h approximately 0.7 GB of data (255.5 GB per year). An image ac-
459 quisition rate of 1 s would increase this figure to approximately 10.4 GB per
460 day (3.8 TB per year). If 25 images are taken every second, one 3 MP camera
461 produces approximately 259 GB of data during 12 h (94.5 TB per year).

462 If only real-time cloud shadow speeds are of interest, the maximum tem-
463 poral resolution is just limited by the calculation time. The required time to
464 derive cloud motion vectors strongly depends on the data transmission rate
465 and can in total be below 1 s, which is faster than the calculations of the CSS.
466 With higher temporal resolutions, the area needed to derive (fast) cloud shadow
467 speeds shrinks. However, as many cloud motion vectors should be measured, the
468 imaged area should not be below a certain minimum. This minimum depends
469 on local characteristics and restrictions as well as the intended application.

470 The CSS however is a fairly compact device, which can be installed at every
471 position which is not shaded by objects. A disadvantage is the detection rate

472 and detection accuracy regarding optically thin clouds. As these clouds are less
473 relevant for e.g. photovoltaic nowcasting applications, this might be acceptable.

474 In direct comparison, the shadow camera obtains more measurements, which
475 scatter less. Also, optically thin clouds can be measured more accurately than
476 with the CSS. Furthermore, the shadow-camera-based approach takes the av-
477 erage cloud motion vector over a larger area, which is more likely to contain
478 cloud shadows than the relatively small area covered by the CSS. Moreover,
479 due to the finite size of cloud shadows, the shadow camera does not face the
480 challenge of the linear cloud edge - curve fitting method as strongly as the CSS
481 (see section A).

482 In general, both systems require little to no maintenance and were found to
483 be robust in the harsh environments present in the desert of Tabernas. Specif-
484 ically, the downward-facing shadow cameras require far less maintenance than
485 the upward-facing all-sky imagers.

486 6. Conclusion and future work

487 On 59 days, the cloud shadow speeds and the cloud directions measured by
488 the CSS are compared to a novel shadow camera approach for two algorithmic
489 methods. For ± 5 min temporal medians, deviations of RMSD 2.1 m/s (28.0 %),
490 MAD 1.2 m/s (15.7 %) and a bias of -0.2 m/s (2.8 %) are found. Deviations of
491 the cloud shadow direction are RMSD 47.9° (26.6 %), MAD 25.3° (14.0 %) and
492 a bias 3.7° (2.0 %). An alternative algorithm, obtaining more measurements,
493 shows higher deviations. In addition to that, the detection rate of the CSS is
494 determined to be between 3.7 % and 21.6 % depending on the shading class on
495 223 days.

496 The effects of the linear cloud edge - curve fitting method are studied and
497 potential solutions discussed. The effects were found to be of minor importance.
498 Potential corrections approaches were found to increase deviations. Thus, we
499 suggest not applying them.

500 As the CSS and the reference shadow camera can be used for the same

501 purposes, the specific advantages and disadvantages are discussed. The CSS
502 is found to be the more flexible tool. However, given certain infrastructural /
503 geographical requirements, the shadow camera might be the better choice. Both
504 systems do not require regular maintenance and come with a small price tag
505 (although the CSS is currently not commercially available).

506 As shown, strict filtering of CSS measurements leads to very little data
507 with many shading events not being measured. If the filtering is less strict,
508 the measurements show larger deviations. Depending on the application, a less
509 accurate measurement might be more desirable than no measurement at all.
510 For instance, if cloud speeds are used to obtain cloud heights for a industri-
511 ally used nowcasting system, less accurate measurements can be preferable to
512 missing measurements. If on the other hand reference data for validations are
513 to be obtained, accuracy might be more important than the total amount of
514 measurements. Therefore, as a software improvement, we suggest making this
515 decision based on the requirements for each application.

516 The CSS used in this study measures for 9 s and stores the results afterwards,
517 which causes a dead time of another 9 s. Although this dead time can be
518 interpolated, continuous measurements would further improve the device. In
519 a redesigned version of the CSS (developed in late 2016), the dead time was
520 reduced to 2 s. Future hardware improvements should further reduce this dead
521 time.

522 In many cases, cloud shadow speeds are not the final measurement of interest
523 but only an intermediate result. Depending on the intended application of
524 the CSS, several other potential hardware adaptations could be implemented.
525 If irradiance values are of interest, one or several sensors of the CSS could
526 be calibrated and thus used to measure GHI. Integrating a rotating shadow
527 band (RSI) into the CSS would further enable direct normal irradiance (DNI)
528 measurements. If the CSS is used as a part of an all-sky imager based nowcasting
529 system or utilized to derive cloud heights, an inexpensive camera could be added,
530 providing a complete system. A CSS and a shadow camera based system, which
531 derives cloud heights, is presented and validated against a ceilometer on the

532 same 59 days in another publication (Kuhn et al., 2018b).

533 In the near future, site evaluations for photovoltaic plants might include
534 mean and maximum cloud speeds as these values impact the size of buffers
535 needed to fulfill ramp rate regulations. The easy-to-deploy CSS can be used to
536 obtain this information.

537 With additional hardware added, the CSS can be upgraded to be a solar
538 nowcasting system in a box, providing irradiance predictions for solar power
539 plants. As currently ramp rate regulations for photovoltaic plants are discussed,
540 which can be fulfilled with the help of nowcasting systems, such systems may
541 support the integration of large solar penetrations into our electricity grids.

542 **Acknowledgements**

543 The research presented in this publication has received funding from the Eu-
544 ropean Union’s Horizon 2020 program for the initial development of the shadow
545 camera system (PreFlexMS, Grant Agreement no. 654984). With founding
546 from the German Federal Ministry for Economic Affairs and Energy within
547 the WobaS project, the shadow camera system was developed. The European
548 Union’s FP7 program under Grant Agreement no. 608623 (DNICast project)
549 financed operations of the all-sky imagers and other ground measurements. The
550 authors are also grateful for the financial support provided by project PRESOL
551 with reference ENE2014-59454-C3-2-R, funded by the Ministerio de Economía y
552 Competitividad and co-financed by the European Regional Development Fund
553 (FEDER). Thanks to the reviewers for their helpful comments and to our col-
554 leagues from the Solar Concentrating Systems Unit of CIEMAT for the support
555 provided in the installation and maintenance of the shadow cameras. These
556 instruments are installed on CIEMAT’s CESA-I tower of the Plataforma Solar
557 de Almería.

558 **Appendix A Angle correction and the linear cloud edge - curve**
559 **fitting method**

560 Here, basic assumptions of the linear cloud edge - curve fitting method are
561 studied and potential solutions discussed. The considerations are not only rele-
562 vant for the CSS, but for many other velocity deriving systems. These investiga-
563 tions require a reference system. The shadow camera provides such references,
564 enabling us to carry out these studies on the CSS. To the best of our knowl-
565 edge, this is the first time such an in-field investigation of the aperture problem
566 is performed.

567 *A.1 The aperture problem on one example day*

568 The aperture problem is a very fundamental challenge for many velocity de-
569 riving systems. Several publications on the CSS and on similar systems (Bosch
570 and Kleissl (2013), Bosch et al. (2013), Lappalainen and Valkealahti (2016a),
571 Lappalainen and Valkealahti (2016b)) use the linear cloud edge method to over-
572 come this problem. In this method, the cloud speed and the moving direction
573 of the cloud are determined from the measurements obtained by two shading
574 flanks with assumed identical cloud motion vectors. To avoid this assumption,
575 the "linear cloud edge - curve fitting method" is implemented in the CSS (Wang
576 et al., 2016). This method assumes that the motion of a cloud is always per-
577 pendicular to the cloud edge (see Fig. 1). If the cloud edge is not perpendicular
578 to the moving direction of the cloud, the cloud speed is underestimated by the
579 factor $\cos \delta$, where δ represents the angle between the speed vector and the nor-
580 mal of the shadow edge. This question has been addressed in previous works
581 but no sufficient answer has been found yet (Bosch et al. (2013), Lappalainen
582 and Valkealahti (2016a)). With the shadow camera acting as a reference, the
583 effects of these systematic deviations can be studied and reversed. Figure A.1
584 visualizes the raw data of the CSS measurements and the shadow camera mea-
585 surements for speed and direction for one example day (2016-04-25) without
586 any temporal averaging for both systems. The CSS measurements scatter in a

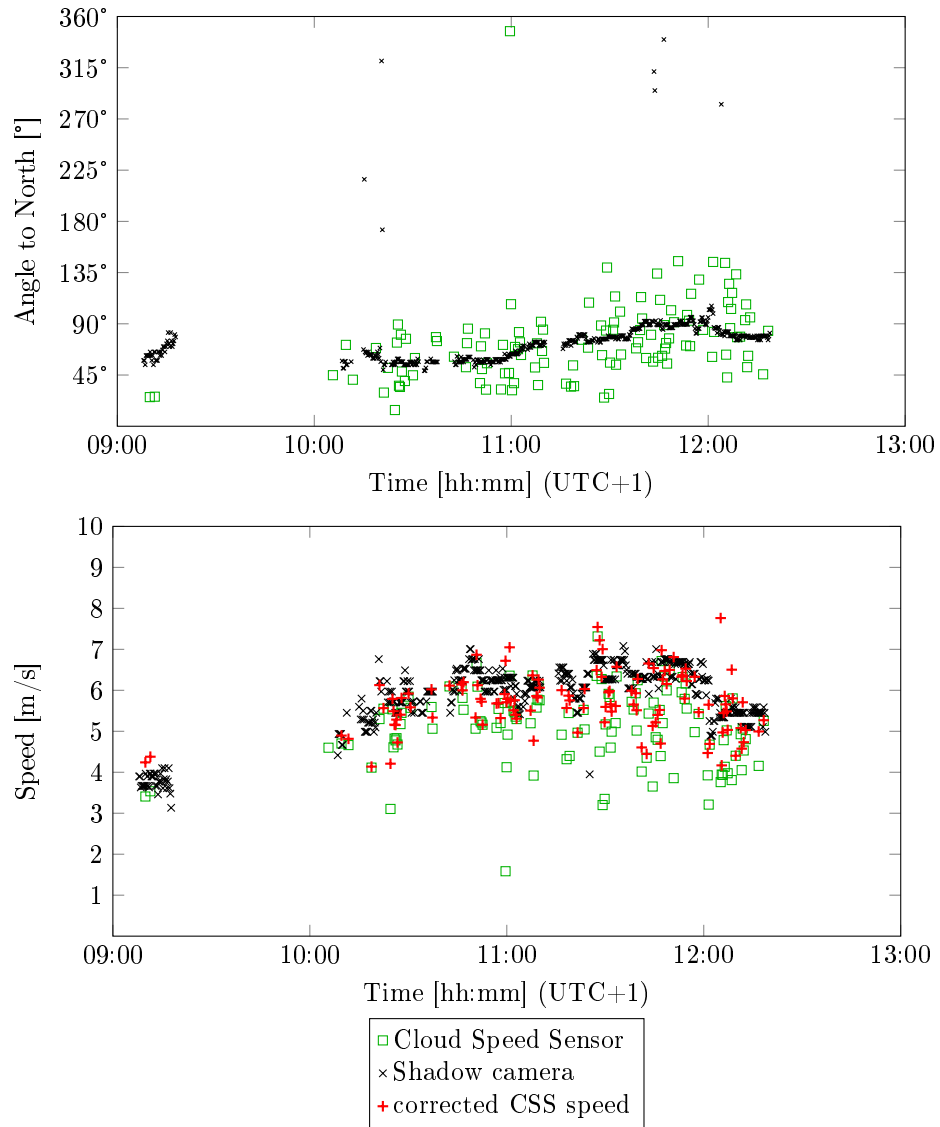


Figure A.1: CSS measurements and the raw data of the shadow camera on 2016-04-25. This example is used to illustrate the effects of the linear cloud edge method.

587 significant range, whereas the shadow camera system cloud motion directions
 588 show almost no scatter at all and only a minor number of outliers throughout
 589 the day. The low level of scatter and bias in the raw data is a strong indica-
 590 tion that the direction detected by the shadow camera is correct. We will show

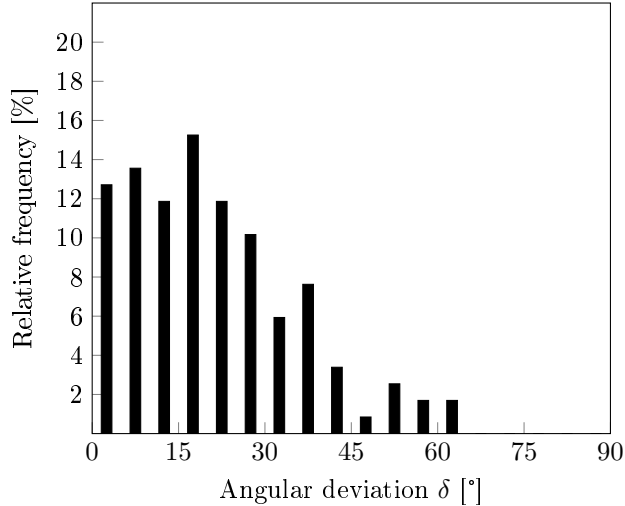


Figure A.2: Angular deviation δ on 2016-04-25 between the one-shadow-camera system and the CSS, depicted for the LSQ method. There is a total of 118 CSS measurements using the LSQ method.

591 in this section that scatter in the CSS data is partially caused by cloud edges
 592 passing the CSS not being perpendicular to the motion vectors.

593 In the following, the moving direction measured by the shadow camera is
 594 considered the true direction of the clouds, which appears justified because its
 595 scatter is very small. The distribution of the thus measured angular deviation
 596 δ between the CSS measurements (displayed for the LSQ method) and the
 597 reference system is shown in Fig. A.2. The deviations are significant and result
 598 in systematically too small speeds as measured by the CSS.

599 With δ known, the CSS speed can be corrected according to equ. A.1 (com-
 600 pare with Fig. 2). The corrected CSS velocities are depicted with + in the
 601 bottom part of Fig. A.1. Due to the correction, the scatter is reduced from
 602 0.9 m/s to 0.7 m/s standard deviation. Furthermore, the corrected average
 603 speed (5.7 m/s) on this day of is closer to the average speed as measured by the
 604 shadow camera (6.2 m/s) than the uncorrected average speed (5.1 m/s).

$$605 \quad v_{CSS}^{corr} = \frac{v_{CSS}}{\cos \delta} \quad (\text{A.1})$$

606 *A.2 Investigating potential solutions*

607 Assuming that the bias (presented in section 4.5) is only caused by $\cos \delta$,
 608 we can calculate the average angular offset $\bar{\delta}_{\text{avg},i}$ using the average velocities
 609 derived with the LSQ and LTS method and equ. A.1, equ. A.2 and equ. A.3.

$$610 \quad \text{bias} = \frac{1}{N} \sum_{i=1}^N (v_{\text{CSS},i} - v_{\text{SC},i}) = \overline{v_{\text{avg,CSS}}} - \overline{v_{\text{avg,SC}}} \quad (\text{A.2})$$

$$611 \quad \cos \bar{\delta}_{\text{avg},i} = \frac{\overline{v_{\text{avg,CSS},i}}}{\overline{v_{\text{avg,CSS},i}} - \text{bias}} \quad (\text{A.3})$$

613 For the LSQ method with an average speed of 8.61 m/s and a bias of -
 614 0.21 m/s for ± 5 min medians, an $\bar{\delta}_{\text{avg,LSQ}} = 12.4^\circ$ is found ($\cos \bar{\delta}_{\text{avg,LSQ}} =$
 615 0.977). For the LTS method (± 5 min medians) with an average speed of 8.48 m/s
 616 and a bias of -0.42 m/s, an $\bar{\delta}_{\text{avg,LTS}} = 17.8^\circ$ is found ($\cos \bar{\delta}_{\text{avg,LTS}} = 0.952$).
 617 However, as we can see in the previous section on one example day, the bias is
 618 not completely caused by δ . Therefore, this effect is arguably not of outmost
 619 importance or hidden behind other deviations.

620 The correction made in the previous section and the bias correction made
 621 here could only be accomplished using a reference measurement system. Several
 622 approaches are possible to make such a correction without reference measure-
 623 ments and will be studied in the following.

624 *A.2.1 Calculate corrections factors based on cloud speeds*

625 A correction approach for $\cos \delta$ based on cloud speeds is discussed (Wang
 626 et al., 2016, section 4.3), but could not be tested due to the lack of a reference
 627 system. Using the shadow camera measurements, this suggested correction is
 628 investigated in this section. The suggested approach can be made operational
 629 by using the maximum velocity measured during a given period of time for all
 630 corresponding measurements. The maximum velocity is thus considered to be
 631 v_{real} . Additionally, this velocity is considered to be perpendicular to the cloud
 632 edge. Both assumptions are questionable.

Table A.1: Cloud speed deviations found for the LSQ and LTS approach with speed-derived corrections applied in comparison to the shadow camera measurements on 59 days.

| | LSQ $_{\pm 2}$ min,corr,max | LSQ $_{\pm 5}$ min,corr,max | LTS $_{\pm 2}$ min,corr,max | LTS $_{\pm 5}$ min,corr,max |
|------|-----------------------------|-----------------------------|-----------------------------|-----------------------------|
| RMSD | 3.1 m/s (41.7 %) | 3.7 m/s (50.8 %) | 3.9 m/s (53.6 %) | 4.7 m/s (64.3 %) |
| MAD | 1.8 m/s (24.0 %) | 2.1 m/s (29.1 %) | 2.4 m/s (32.5 %) | 3.0 m/s (40.3 %) |
| bias | 1.0 m/s (+14.0 %) | 1.6 m/s (+22.9 %) | 1.4 m/s (+19.2 %) | 2.4 m/s (+32.0 %) |

633 Table A.1 shows the deviations found if the maximum speed measured in a
634 period of time is compared to the medians of the shadow camera for the same
635 period. In comparison to Tab. 8, in which the deviations without this correction
636 are presented, the deviations shown here are significantly larger. Especially the
637 bias, which is now positive, is increased by this correction. The larger deviations
638 are caused by the scatter present in the CSS measurements (visualized in the
639 plots of section 4.1). Moreover, cloud speeds might change significantly within
640 ± 5 min. Thus, this correction approach is not feasible.

641 A.2.2 Calculate corrections factors based on cloud directions

642 Another approach to derive correction factors for cloud speeds not perpen-
643 dicular to the corresponding cloud edges is based on the directions. For a period
644 of time, a median cloud motion direction is calculated. This way, $\cos \delta$ can be
645 estimated for every measurement and the velocities can be corrected. Thus
646 derived, δ is Gaussian distribution with a standard deviation of e.g. 52.8° for
647 LSQ $_{\pm 2}$ min,corr.

648 In Tab. A.2, the deviations in comparison to the shadow camera measure-
649 ments are shown. Offsets greater than one standard deviation are not corrected.
650 Including these corrections leads to higher deviations. The velocities are not fur-
651 ther temporally averaged within the considered time periods.

652 In comparison to Tab. 8, Tab. A.2 shows higher deviations. Increasing the
653 period of time to calculate the median cloud motion vectors from ± 2 min to
654 ± 5 min increases the RMSD and MAD. Notably, the bias is reduced. In sum-
655 mary, we conclude that this correction approach is not feasible. The reason for

Table A.2: Cloud speed deviations found for the LSQ and LTS approach with direction-derived corrections applied in comparison to the shadow camera measurements on 59 days. δ above one standard deviation are not corrected. The velocities are not further temporally averaged within the considered time periods.

| | LSQ $_{\pm 2}$ min,corr | LSQ $_{\pm 5}$ min,corr | LTS $_{\pm 2}$ min,corr | LTS $_{\pm 5}$ min,corr |
|------|-------------------------|-------------------------|-------------------------|-------------------------|
| RMSD | 2.8 m/s (37.7 %) | 2.8 m/s (37.6 %) | 3.5 m/s (47.6 %) | 3.6 m/s (49.3 %) |
| MAD | 1.6 m/s (22.4 %) | 1.7 m/s (22.8 %) | 2.1 m/s (28.9 %) | 2.2 m/s (30.3 %) |
| bias | +0.1 m/s (+1.2 %) | +0.2 m/s (2.5 %) | -0.1 m/s (-1.2 %) | -0.02 m/s (-0.3 %) |

656 this is, similar as discussed in the previous section, the scatter of the CSS mea-
657 surements. Furthermore, it is a mere assumption that the median cloud motion
658 vector itself is perpendicular to the cloud edge.

659 A.2.3 Assuming circular clouds

660 The angular offset δ can be corrected if the shape and the size of each cloud
661 is known. In this section, this approach is investigated by calculating backwards
662 using $\bar{\delta}_{\text{avg},i}$ derived earlier at the beginning of section A.2. Figure A.3 visualizes
663 the situation. A circular cloud with unknown radius R is approaching the CSS
664 from one particular direction. The distance D is 29.7 cm (see Fig. 1b) and we use
665 $\delta = \bar{\delta}_{\text{avg,LSQ}} = 12.4^\circ$ for this example calculation. Thus, x can be derived to be
666 6.5 cm. β is defined by $\sin \beta = \frac{D}{R}$ and $\cos \beta = \frac{R-x}{R}$. Using $(\sin \beta)^2 + (\cos \beta)^2 = 1$,
667 the radius can be determined to be $R = 70.8$ cm. Hypothetically, this radius may
668 correspond to intra-cloud structures and is far too small for usual cloud sizes. As
669 both the shape (here: circular) and the size of the clouds/intra-cloud structures
670 must be assumed to achieve this correction, this approach is not feasible. The
671 calculations shown in this section are included for further understanding of the
672 general problem.

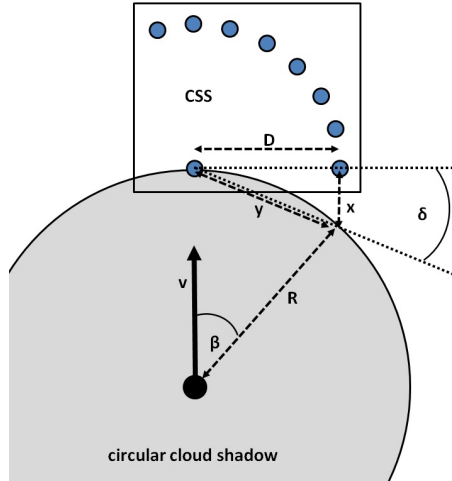


Figure A.3: Visualization of the circular cloud assumption to correct δ .

673 *A.3 Concluding remarks: Linear cloud edge - curve fitting method*

674 Here, a fundamental challenge within the linear cloud edge - curve fitting
 675 method was studied and several correction approaches investigated. All consid-
 676 ered correction approaches increase deviations in comparison to shadow camera
 677 reference measurements. It was found that in general, the deviations caused by
 678 non-perpendicular cloud motion vectors are, at least for the weather conditions
 679 considered here, of minor importance. We therefore suggest not to apply the
 680 presented correction approaches. However, we like to stress that these offsets
 681 must be kept in mind.

682 **References**

683 **References**

684 Bloomfield, P., Steiger, W., 2012. Least absolute deviations: Theory, applica-
 685 tions and algorithms. volume 6. Springer Science & Business Media.

686 Bosch, J.L., Kleissl, J., 2013. Cloud motion vectors from a network of ground
 687 sensors in a solar power plant. Solar Energy 95, 13–20. URL: <http://dx.doi.org>.

- 688 [org/10.1016/j.solener.2013.05.027](http://dx.doi.org/10.1016/j.solener.2013.05.027), doi:10.1016/j.solener.2013.05.
689 027.
- 690 Bosch, J.L., Zheng, Y., Kleissl, J., 2013. Deriving cloud velocity from
691 an array of solar radiation measurements. *Solar Energy* 87, 196–
692 203. URL: <http://dx.doi.org/10.1016/j.solener.2012.10.020>, doi:10.
693 1016/j.solener.2012.10.020.
- 694 Chen, X., Du, Y., Wen, H., 2017. Forecasting based power ramp-rate con-
695 trol for PV systems without energy storage, in: 2017 IEEE 3rd Interna-
696 tional Future Energy Electronics Conference and ECCE Asia (IFEEC 2017 -
697 ECCE Asia), pp. 733–738. URL: [http://ieeexplore.ieee.org/abstract/
698 document/7992130/](http://ieeexplore.ieee.org/abstract/document/7992130/), doi:10.1109/IFEEC.2017.7992130.
- 699 Fung, V., Bosch, J.L., Roberts, S.W., Kleissl, J., 2013. Cloud shadow speed
700 sensor. *Atmospheric Measurement Techniques* 6. URL: [http://dx.doi.org/
701 10.5194/amt-7-1693-2014](http://dx.doi.org/10.5194/amt-7-1693-2014), doi:10.5194/amt-7-1693-2014.
- 702 Giloni, A., Padberg, M., 2002. Least Trimmed Squares Regression, Least Me-
703 dian Squares Regression, and Mathematical Programming. *Mathematical and
704 Computer Modelling* 35, 1043–1060. URL: [http://dx.doi.org/10.1016/
705 S0895-7177\(02\)00069-9](http://dx.doi.org/10.1016/S0895-7177(02)00069-9), doi:10.1016/S0895-7177(02)00069-9.
- 706 Hanrieder, N., Sengupta, M., Xie, Y., Wilbert, S., Pitz-Paal, R., 2016. Modeling
707 beam attenuation in solar tower plants using common DNI measurements. *So-
708 lar Energy* 129, 244–255. URL: [http://www.sciencedirect.com/science/
709 article/pii/S0038092X1600075X](http://www.sciencedirect.com/science/article/pii/S0038092X1600075X).
- 710 Huang, H., Yoo, S., Yu, D., Huang, D., Qin, H., 2012. Correlation and lo-
711 cal feature based cloud motion estimation, in: *Proceedings of the Twelfth
712 International Workshop on Multimedia Data Mining*, ACM, New York,
713 NY, USA. pp. 1–9. URL: <http://doi.acm.org/10.1145/2343862.2343863>,
714 doi:10.1145/2343862.2343863.
- 715 Huber, P.J., 2009. *Robust Statistics*. Springer.

- 716 Killius, N., Prah, C., Hanrieder, N., Wilbert, S., Schroedter-Homscheidt, M.,
717 2015. On the use of NWP for Cloud Base Height Estimation in Cloud Camera-
718 Based Solar Irradiance Nowcasting. URL: [http://www.wemcouncil.org/wp/
719 wp-content/uploads/2015/07/1510_MarionSchroedterHomscheidt.pdf](http://www.wemcouncil.org/wp/wp-content/uploads/2015/07/1510_MarionSchroedterHomscheidt.pdf).
720 oral presentation on EUPVSEC.
- 721 Klein, S.A., Jakob, C., 1999. Validation and Sensitivities of Frontal
722 Clouds Simulated by the ECMWF Model. Monthly Weather Review
723 127, 2514–2531. URL: [http://journals.ametsoc.org/doi/abs/10.1175/
724 1520-0493\(1999\)127%3C2514%3AVAS0FC%3E2.0.CO%3B2](http://journals.ametsoc.org/doi/abs/10.1175/1520-0493(1999)127%3C2514%3AVAS0FC%3E2.0.CO%3B2).
- 725 Kuhn, P., Nouri, B., Wilbert, S., Prah, C., Kozonek, N., Schmidt, T., Yasser,
726 Z., Ramirez, L., Zarzalejo, L., Meyer, A., Vuilleumier, L., Heinemann, D.,
727 Blanc, P., Pitz-Paal, R., 2017a. Validation of an all-sky imager-based now-
728 casting system for industrial PV plants. Progress in Photovoltaics: Research
729 and Applications , n/a–n/aURL: <http://dx.doi.org/10.1002/pip.2968>,
730 doi:10.1002/pip.2968. pIP-17-122.R1.
- 731 Kuhn, P., Wilbert, S., Prah, C., Garsche, D., Schüler, D., Haase, T., Ramirez,
732 L., Zarzalejo, L., Meyer, A., Blanc, P., Pitz-Paal, R., 2018a. Applications of
733 a shadow camera system for energy meteorology. Advances in Science and
734 Research 15, 11–14. URL: <https://www.adv-sci-res.net/15/11/2018/>,
735 doi:10.5194/asr-15-11-2018.
- 736 Kuhn, P., Wilbert, S., Prah, C., Schüler, D., Haase, T., Hirsch,
737 T., Wittmann, M., Ramirez, L., Zerzalejo, L., Meyer, A., Vuilleu-
738 mier, L., Blanc, P., Pitz-Paal, R., 2017b. Shadow camera system
739 for the generation of solar irradiance maps. Solar Energy 157, 157
740 – 170. URL: [http://www.sciencedirect.com/science/article/pii/
741 S0038092X17304814](http://www.sciencedirect.com/science/article/pii/S0038092X17304814), doi:[https://doi.org/10.1016/j.solener.2017.05.
742 074](https://doi.org/10.1016/j.solener.2017.05.074).
- 743 Kuhn, P., Wilbert, S., Schüler, D., Prah, C., Haase, T., Ramirez, L., Zarza-
744 lejo, L., Meyer, A., Vuilleumier, L., Blanc, P., Dubrana, J., Kazantzidis,

745 A., Schroedter-Homscheidt, M., Hirsch, T., Pitz-Paal, R., 2017c. Validation
746 of spatially resolved all sky imager derived DNI nowcasts. AIP Conference
747 Proceedings 1850, 140014. URL: [http://aip.scitation.org/doi/abs/10.](http://aip.scitation.org/doi/abs/10.1063/1.4984522)
748 [1063/1.4984522](http://aip.scitation.org/doi/abs/10.1063/1.4984522), doi:10.1063/1.4984522.

749 Kuhn, P., Wirtz, M., Killius, N., Wilbert, S., Bosch, J., Hanrieder, N.,
750 Nouri, B., Kleissl, J., Ramirez, L., Schroedter-Homscheidt, M., Heine-
751 mann, D., Kazantzidis, A., Blanc, P., Pitz-Paal, R., 2018b. Bench-
752 marking three low-cost, low-maintenance cloud height measurement sys-
753 tems and ECMWF cloud heights against a ceilometer. Solar En-
754 ergy , -URL: [https://www.sciencedirect.com/science/article/pii/](https://www.sciencedirect.com/science/article/pii/S0038092X1830183X)
755 [S0038092X1830183X](https://www.sciencedirect.com/science/article/pii/S0038092X1830183X), doi:[https://doi.org/10.1016/j.solener.2018.02.](https://doi.org/10.1016/j.solener.2018.02.050)
756 [050](https://doi.org/10.1016/j.solener.2018.02.050).

757 Lappalainen, K., Valkealahti, S., 2016a. Analysis of shading periods caused by
758 moving clouds. Solar Energy 135, 188–196. URL: [http://dx.doi.org/10.](http://dx.doi.org/10.1016/j.solener.2016.05.050)
759 [1016/j.solener.2016.05.050](http://dx.doi.org/10.1016/j.solener.2016.05.050), doi:10.1016/j.solener.2016.05.050.

760 Lappalainen, K., Valkealahti, S., 2016b. Apparent velocity of shadow edges
761 caused by moving clouds. Solar Energy 138, 47–52. URL: [http://dx.doi.](http://dx.doi.org/10.1016/j.solener.2016.09.008)
762 [org/10.1016/j.solener.2016.09.008](http://dx.doi.org/10.1016/j.solener.2016.09.008), doi:10.1016/j.solener.2016.09.
763 [008](http://dx.doi.org/10.1016/j.solener.2016.09.008).

764 Lave, M., Kleissl, J., Ellis, A., Mejia, F., 2013. Simulated PV power plant
765 variability: Impact of utility-imposed ramp limitations in Puerto Rico, in:
766 2013 IEEE 39th Photovoltaic Specialists Conference (PVSC), pp. 1817–
767 1821. URL: <http://ieeexplore.ieee.org/document/6744495/>, doi:10.
768 [1109/PVSC.2013.6744495](http://ieeexplore.ieee.org/document/6744495/).

769 Mäki, A., Valkealahti, S., 2012. Power Losses in Long String and Parallel-
770 Connected Short Strings of Series-Connected Silicon-Based Photovoltaic
771 Modules Due to Partial Shading Conditions. IEEE Transactions on Energy
772 Conversion 27, 173–183. URL: [http://dx.doi.org/10.1109/TEC.2011.](http://dx.doi.org/10.1109/TEC.2011.2175928)
773 [2175928](http://dx.doi.org/10.1109/TEC.2011.2175928), doi:10.1109/TEC.2011.2175928.

- 774 Marcos, J., l, O.S., Marroyo, L., Garcia, M., Lorenzo, E., 2014. Stor-
775 age requirements for PV power ramp-rate control. *Solar Energy*
776 99, 28 – 35. URL: [http://www.sciencedirect.com/science/article/
777 pii/S0038092X13004672](http://www.sciencedirect.com/science/article/pii/S0038092X13004672), doi:[http://doi.org/10.1016/j.solener.2013.
778 10.037](http://doi.org/10.1016/j.solener.2013.10.037).
- 779 Molteni, F., Buizza, R., Palmer, T.N., Petroliaqis, T., 1996. The ECMWF
780 Ensemble Prediction System: Methodology and validation. *Quarterly Journal*
781 of the Royal Meteorological Society 122, 73–119. URL: [http://dx.doi.org/
782 10.1002/qj.49712252905](http://dx.doi.org/10.1002/qj.49712252905), doi:10.1002/qj.49712252905.
- 783 Mount, D.M., Netanyahu, N.S., Piatko, C.D., Silverman, R., Wu, A.Y.,
784 2014. On the Least Trimmed Squares Estimator. *Algorithmica* 69,
785 148–183. URL: <http://dx.doi.org/10.1007/s00453-012-9721-8>, doi:10.
786 1007/s00453-012-9721-8.
- 787 Rousseeuw, P.J., 1984. Least median of squares regression. *Journal of the*
788 *American statistical association* 79, 871–880. URL: [http://dx.doi.org/10.
789 2307/2288718](http://dx.doi.org/10.2307/2288718), doi:10.2307/2288718.
- 790 Rousseeuw, P.J., Croux, C., 1993. Alternatives to the median abso-
791 lute deviation. *Journal of the American Statistical association* 88,
792 1273–1283. URL: <http://dx.doi.org/10.1080/01621459.1993.10476408>,
793 doi:10.1080/01621459.1993.10476408.
- 794 Scaramuzza, D., Martinelli, A., Siegwart, R., 2006. A toolbox for easily calibrat-
795 ing omnidirectional cameras, in: 2006 IEEE/RSJ International Conference
796 on Intelligent Robots and Systems, IEEE. pp. 5695–5701. URL: [http://
797 ieeexplore.ieee.org/abstract/document/4059340/](http://ieeexplore.ieee.org/abstract/document/4059340/), doi:10.1109/IR0S.
798 2006.282372.
- 799 Schenk, H., Hirsch, T., Wittmann, M., Wilbert, S., Keller, L., Prah1, C., 2015.
800 Design and Operation of an Irradiance Measurement Network. *Energy Pro-*
801 *cedia* 69, 2019–2030. URL: [http://dx.doi.org/10.1016/j.egypro.2015.
802 03.212](http://dx.doi.org/10.1016/j.egypro.2015.03.212), doi:10.1016/j.egypro.2015.03.212.

- 803 Tomassini, M., Kelly, G., Saunders, R., 1999. Use and Impact of Satellite
804 Atmospheric Motion Winds on ECMWF Analyses and Forecasts. Monthly
805 Weather Review 127, 971–986. URL: [http://journals.ametsoc.org/doi/
806 full/10.1175/1520-0493\(1999\)127%3C0971%3AUAI0SA%3E2.O.CO%3B2](http://journals.ametsoc.org/doi/full/10.1175/1520-0493(1999)127%3C0971%3AUAI0SA%3E2.O.CO%3B2).
- 807 Wang, G., Kurtz, B., Kleissl, J., 2016. Cloud base height from sky imager and
808 cloud speed sensor. Solar Energy 131, 208–221. URL: [http://dx.doi.org/
809 10.1016/j.solener.2016.02.027](http://dx.doi.org/10.1016/j.solener.2016.02.027), doi:10.1016/j.solener.2016.02.027.